Anisotropic stress orients remodelling of mammalian limb bud ectoderm

Kimberly Lau[1,11], Hirotaka Tao[1,11], Haijiao Liu[2,3], Jun Wen[2], Kendra Sturgeon[1], Natalie Sorfazlian[1], Savo Lazic[1,4], Jeffrey T. A. Burrows[1], Michael D. Wong[5,6], Danyi Li[1,4], Steven Deimling[1], Brian Ciruna[1,4], Ian Scott[1,4], Craig Simmons[2,3], R. Mark Henkelman[5,6], Trevor Williams[7], Anna-Katerina Hadjantonakis[8], Rodrigo Fernandez-Gonzalez[3,9], Yu Sun[2,3] and Sevan Hopyan[1,4,10,12]

The physical forces that drive morphogenesis are not well characterized *in vivo*, especially among vertebrates. In the early limb bud, dorsal and ventral ectoderm converge to form the apical ectodermal ridge (AER), although the underlying mechanisms are unclear. By live imaging mouse embryos, we show that prospective AER progenitors intercalate at the dorsoventral boundary and that ectoderm remodels by concomitant cell division and neighbour exchange. Mesodermal expansion and ectodermal tension together generate a dorsoventrally biased stress pattern that orients ectodermal remodelling. Polarized distribution of cortical actin reflects this stress pattern in a β-catenin- and Fgfr2-dependent manner. Intercalation of AER progenitors generates a tensile gradient that reorients resolution of multicellular rosettes on adjacent surfaces, a process facilitated by β-catenin-dependent attachment of cortex to membrane. Therefore, feedback between tissue stress pattern and cell intercalations remodels mammalian ectoderm.

It has long been recognized that physical forces underlie embryonic shape changes[1]. New insights based on theory and experiment are progressively decorating this concept with exciting details[2]. However, many aspects of how forces relate to cell behaviours and how interplay between different tissues physically shapes embryonic structures remain unclear, especially among vertebrates. The limb bud derives from the lateral plate and is initially composed of a mesodermal core that is surrounded by a single cell layer of ectoderm. Mesodermal growth initiates limb development and is characterized by oriented cell behaviours that promote elongation of the proximodistal (PD) axis[3–6]. It has been postulated that early ectoderm and the AER, a stratified epithelial signalling centre that is essential for outgrowth and pattern formation[7], might help to maintain a narrow dorsoventral (DV) bud axis[8,9].

AER formation requires, in part, a signal relay between mesodermal and ectodermal cells that activates canonical Wnt and Fgfr2 signalling in ectoderm[10–14]. The importance of these pathways is underscored by mutations that cause limb deficiencies in humans including tetra-amelia and Apert syndrome[15,16]. In the mouse embryo,

AER precursors derive from a broad domain of primarily ventral ectoderm that transitions from cuboidal to columnar morphology[17] and converges just ventral to the DV boundary[18–21]. Although it is not clear what underlies this convergence, one possibility suggested previously is that coordinated cell rearrangements drive AER progenitors to move towards the DV compartment boundary[22]. Here we present evidence that supports this concept, and show that both mesodermal and ectodermal forces contribute to the ectodermal stress pattern that guides multicellular remodelling. Our findings suggest that β-catenin and Fgfr2 in part mediate cellular responses to tissue forces.

RESULTS

Cell topology and intercalation of prospective AER progenitors

Cell intercalation is associated with non-hexagonal cell topology[23]. Using whole-mount immunostaining, we observed that ectodermal cells in the pre-AER limb field (20 som. (somite stage)) of the mouse embryo exhibited a wide range of topologies (Fig. 1a). The distribution of cell interfaces (number of cell neighbours) was centred on five
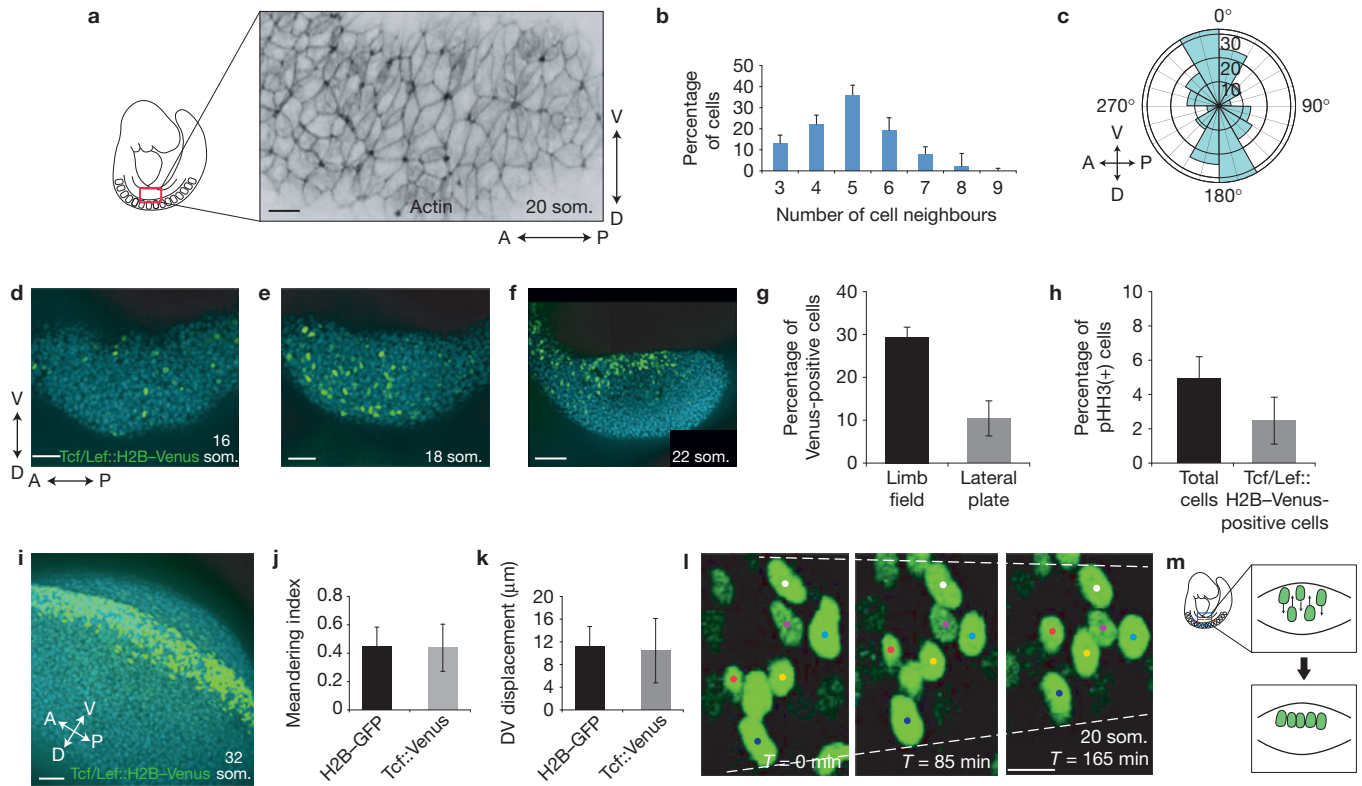
Figure 1 Cell topology and intercalation of AER progenitors. (**a**) Confocal section of rhodamine–phalloidin-stained pre-AER (20 som.) entire limb field (from somite 7 to 11, ~250 ectodermal cells) demonstrating variable and non-hexagonal cell topologies as well as DV elongation of some ectodermal cells (quantified in Supplementary Figs 4 and 5). (**b**) Distribution of number of cell neighbours among 18–20 som. limb bud ectodermal cells. (**c**) Polar plot representing metaphase-to-telophase transition angles of limb bud ectoderm cells ($n = 3$, 35–40 cell divisions (all cell divisions/2 h time-lapse video) per 18–20 som. embryo). (**d–f**) Confocal projection of the ectodermal *Tcf/Lef::H2B–Venus* reporter in pre-overt initiation limb field (16 som.; **d**), early initiating limb field (18 som.; **e**), and post-initiation limb field (22 som.; **f**) (blue: DAPI). (**g**) Percentage of Tcf/Lef::H2B–Venus-positive cells in the limb field versus lateral plate in 18–20 som. embryos ($n = 3$ embryos; $P = 0.0022$ (Student's *t*-test)). (**h**) Percentage of pHH3-positive cells relative to total cells versus percentage of pHH3-positive cells relative to Tcf/Lef::H2B–Venus-positive cells in the limb field in 18–20 som. embryos ($n = 3$ embryos; $P = 0.26$ (Student's *t*-test)). (**i**) Confocal projection of the ectodermal *Tcf/Lef::H2B–Venus* reporter in an AER-forming limb bud (32 som.). (**j**,**k**) Meandering index (**j**) and DV displacement (**k**) among ubiquitously expressed H2B–GFP (representing total cells) versus Tcf/Lef::H2B–Venus (representing AER progenitors) cells in 18–20 som. embryos ($n = 20$ cells in 3 embryos for each condition; (**j**) $P = 0.86$, (**k**) $P = 0.74$ (Student's *t*-test)). (**l**) Time-lapse series of a 20 som. limb bud ectoderm expressing *Tcf/Lef::H2B–Venus* near the DV boundary. Dashed lines highlight regional tissue constriction. (**m**) Model of AER progenitor intercalation just ventral to the DV boundary (red line). Scale bars indicate 10 μm (**a**,**l**), 50 μm (**d**,**e**,**i**), 100 μm (**f**). Error bars indicate s.e.m.

and is shifted to the left compared with a common distribution centred on six interfaces that was previously described for invertebrate and earlier vertebrate embryos[24] (Fig. 1b). This finding suggests that some cell behaviours in the mouse embryo may be distinct to those observed in other metazoa. During early limb development (20 som.), ectodermal cells within the limb field became elongated along the DV axis (Fig. 1a), suggesting that they were under tension. By live imaging 18–20 som. *CAG::H2B–EGFP* reporter embryos that ubiquitously express nuclear EGFP (ref. 25), we found that cell division orientation was biased dorsoventrally in limb field and non-limb lateral plate ectoderm (Fig. 1c). By themselves, these cell behaviours would expand the DV axis of at least the ectodermal layer. Therefore, compensatory cell rearrangements may be important to accommodate new cells without distorting tissue shape.

As canonical Wnt signalling is essential for AER formation, we employed the transgenic nuclear reporter *Tcf/Lef::H2B–Venus* to monitor canonical Wnt activation in limb bud cells[26]. This reporter

was activated infrequently in the limb field before overt limb initiation (16 som., <E9.0; Fig. 1d). The number of *Tcf/Lef*-positive cells increased in limb field ectoderm once bud growth was underway (>18 som., ~E9.0; Fig. 1e,f), but not in non-limb lateral plate ectoderm (Fig. 1g). The proportion of phospho-histone H3 (pHH3)-stained cells was similar between *Tcf/Lef*-positive and -negative cells (Fig. 1h and Supplementary Fig. 1a), suggesting that this increase was not due to a proliferative advantage but rather to differentiation. *Tcf/Lef*-positive cells were initially found in a broad DV domain (as are AER progenitors in the chick embryo[22]) and, consistent with previous lineage tracing of AER progenitors in mouse[17,20], became biased to the ventral surface between the 18 and 22 som. stages (Fig. 1f) before accumulating in the nascent AER (32 som., ~E10.0; Fig. 1i). This ventral cell compaction is comparable to changes in the domain of *Fgf8* expression (an AER marker)[7] and was proposed in a previous model[20]. Although the *Tcf/Lef* signal is not an indelible label for AER progenitors, we noted that it was not selectively
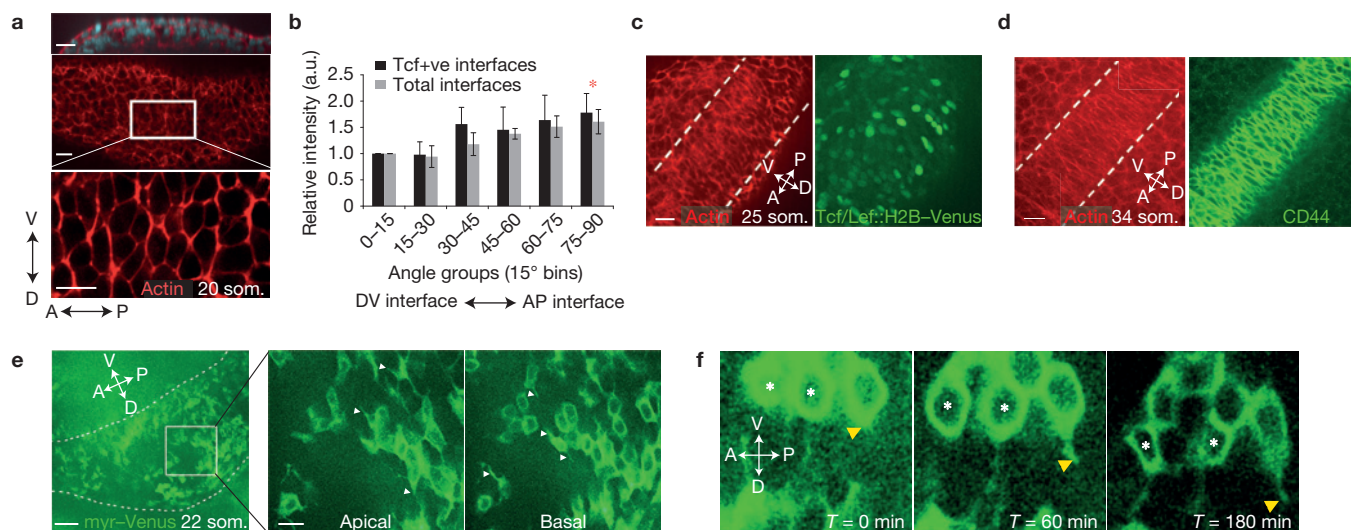
Figure 2 Planar polarity of pre-AER ectodermal cells. (**a**) Confocal *xz* (top) and *xy* (middle and bottom) sections of rhodamine–phalloidin-stained 20 som. limb bud ectoderm highlight the basal region where actin was polarized. (**b**) Relative fluorescence intensity of actin at cell interfaces was analysed using SIESTA software and plotted from 0–90° representing DV to AP interfaces of 18–20 som. embryos ($P = 0.03$ (total interfaces) and $P = 0.05$ (Tcf+ve interfaces) (Student's *t*-test)). Shown are total cell interfaces versus Tcf/Lef::H2B–Venus-positive cell interfaces ($n = 5$ embryos for each condition; comparison of total interfaces versus Tcf/Lef::H2B–Venus-positive cell interfaces $P > 0.05$ for all angle bins (Student's *t*-test)). (**c**,**d**) Confocal image of the basal layer of the nascent AER (between dashed lines) at 25 som. (**c**) and 34 som. (**d**) showing actin (red) and Tcf/Lef::H2B–Venus (green; **c**) or AER marker CD44 (green; **d**; ref. 55). (**e**) Confocal section of a 22 som. limb bud expressing *myr–Venus*. Dashed lines indicate limb bud area. The outlined area is shown magnified in the middle and right panels. Shown are apical and basal sections of the same region. White arrowheads indicate membrane protrusions. (**f**) Confocal time series of a 22 som. limb bud expressing *myr–Venus*, showing protrusive activity along the DV axis (indicated by yellow arrowheads). Intercalation is observed between two cells marked with white asterisks. Scale bars indicate 50 μm (**e**), 20 μm (**a**,**c**–**e** (magnifications)), 10 μm (**f**). Error bars indicate s.e.m. Asterisks indicate $P < 0.05$ (75–90° bin versus 0–15° bin).

extinguished among dorsal cells during 1–3 h live imaging sessions. Rather, cells moved along the DV axis (Supplementary Video 1). Interestingly, *Tcf/Lef*-positive and -negative cells travelled and meandered (displacement/total distance travelled)[27] to a similar extent (Fig. 1j,k), indicating that preferential migration does not explain the accumulation of AER cells near the DV boundary. Instead, ectodermal sheets gradually converged, suggesting that ectodermal cells were planar polarized. At the site of the prospective AER that is just ventral to the DV boundary in the mouse in our estimation, tracked cells interdigitated in time-lapse videos (Fig. 1l,m and Supplementary Videos 2 and 3). Therefore, oriented DV movement and intercalation of cells accompanies formation of the AER.

Planar polarity of pre-AER ectodermal cells

Polarized accumulation of filamentous (F) actin and/or non-muscle myosin type II[28,29] can orient cell movements. Using the program SIESTA (ref. 30) we found that basolateral cortical F-actin was enriched at ectodermal anterior–posterior (AP) interfaces in a broad DV region in the 20 som. pre-AER limb bud and is consistent with the DV axis of cell intercalation (Fig. 2a,b). Cells with polarized actin became progressively confined to the DV midline (Fig. 2c) and nascent AER as shown at the 34 som. stage (Fig. 2d). To examine the importance of polarized actin, we performed roller culture of whole mouse embryos in the presence of the Rac1 inhibitor NSC23766 (ref. 31). This compound abolished actin polarity, diminished the degree of elongated and anisotropic cell topologies and inhibited cell movements (Supplementary Fig. 1b and Supplementary Videos 4

and 5). Organized cell behaviours therefore require Rac1-dependent actin. Unexpectedly, distributions of myosin IIB, IIA and phospho-myosin light chain (pMLC) were largely cortical but not polarized at any stage leading up to AER formation (Supplementary Fig. 1c–e). It is possible that an atypical myosin is polarized here, or that polarized cortical actin is sufficient to bias myosin motor activity.

If pure *Drosophila*-like contractile intercalation secondary to planar polarized actomyosin underlay early AER formation, we would have expected AP cell interfaces to gradually shorten[30,31]. However, activation of the transgenic live actin reporter *R26R:Venus–actin*[32] in ectoderm using an early ectoderm-specific Cre recombinase, *Crect*[33], revealed that, although cell interface lengths oscillated, average AP cell interfaces did not shorten progressively during intercalation at the DV midline (average 25 som. stage AP cell interface length at $T = 0$ min and $T = 120$ min: 7.44 μm ± 0.34 μm (s.e.m.) and 6.75 μm ± 0.5 μm (s.e.m.), respectively; $P = 0.260$). Maintenance of long AP interface lengths was also apparent in static images of the prospective AER (Fig. 2c,d). To investigate the possibility that *Xenopus*-like cell crawling[34] contributes to AER progenitor intercalation, we examined transgenic animals in our colony in which expression of the membrane reporter *CAG::myr–Venus* (ref. 35) had become mosaic. We identified dorsal and ventral protrusions among pre-AER ectodermal cells that spanned the lateral membrane from apical to basal levels (Fig. 2e). Interestingly, live observation demonstrated that protrusive activity took place concurrently with cell intercalations (Fig. 2f and Supplementary Video 6; consistent with Fig. 1j,k). We therefore propose that, similar to mouse neural plate[36], ectoderm remodels
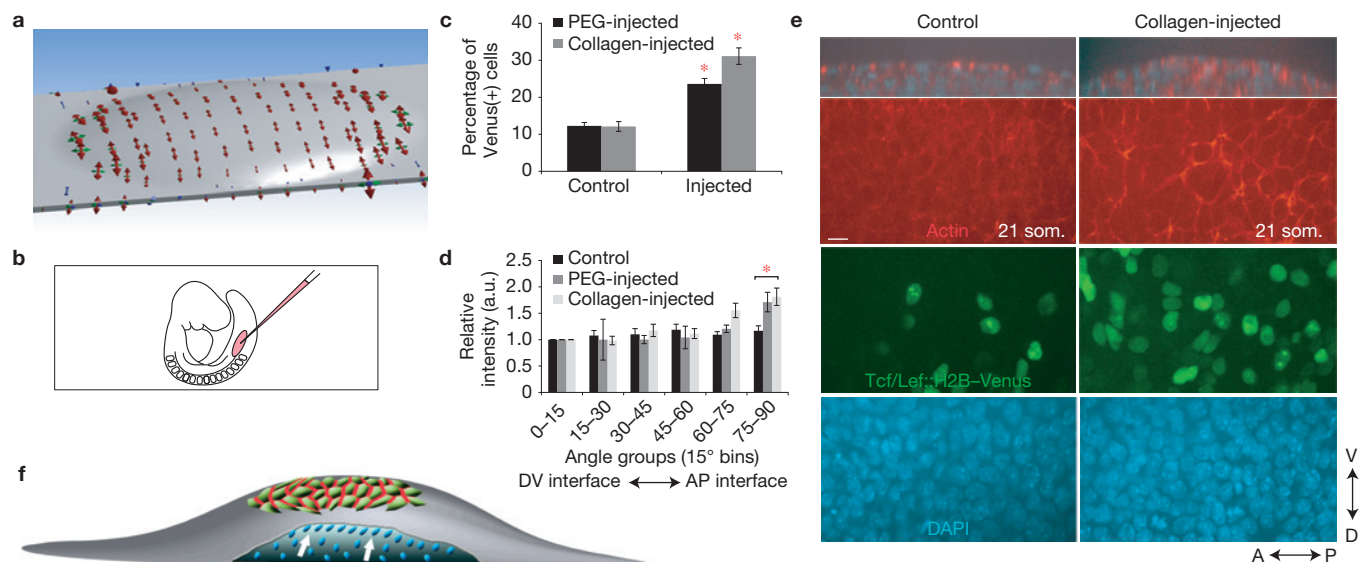
571

Figure 3 Mesodermal growth anisotropically stresses ectoderm during limb initiation. (**a**) Finite-element simulated principal stresses that are attributable to mesodermal growth at limb initiation (17 som.). Red, green and blue arrows indicate maximum, middle and minimum principal stresses respectively. Tension is biased along the DV axis. (**b**) Illustration indicating flank micro-injection in non-limb lateral plate mesoderm. (**c**) Proportion of Venus-positive nuclei in PEG-injected or collagen-injected flank ectoderm compared with control penetrated but uninjected flank ectoderm of 18–21 som. *Tcf/Lef::H2B–Venus* embryos ($n = 3$ embryos per condition, $P = 0.0018$ (collagen)-; $P = 7.2 \times 10^{-6}$ (PEG)-injected versus control (Student's *t*-test)). (**d**) Relative fluorescence intensity of actin at cell interfaces was quantified using SIESTA software and plotted over 90° ($n = 3$ embryos per condition; $P = 0.0021$ (collagen)-; $P = 0.025$ (PEG)-injected versus control (Student's *t*-test)). (**e**) Confocal images of control and collagen-injected 21 som. *Tcf/Lef::H2B–Venus* flank ectoderm. Shown are *z* sections (top panels) and *xy* sections visualizing actin (red), H2B–Venus (green) and DAPI (blue). (**f**) Limb initiation model. Mesodermal growth at limb initiation (blue; white arrows indicate direction of mesodermal growth) is sufficient to anisotropically stress the overlying ectoderm owing to the elongate shape of the lateral plate, resulting in accumulation of actin (red) at AP cell interfaces. Scale bar, 10 μm (**e**). Error bars indicate s.e.m. Asterisks indicate $P < 0.05$ (**d**), $P < 0.01$ (**c**).

through cell rearrangements that are oriented by planar polarized actin and facilitated by protrusive behaviour.

Mesodermal growth anisotropically stresses ectoderm during limb initiation

As tension induces structural changes of F-actin[37], we studied whether mesodermal growth that initiates limb development causes tension in the overlying ectoderm. We employed three-dimensional (3D) finite-element modelling of the initial 17 som. limb field by incorporating actual lateral plate ectoderm dimensions, Young's modulus that we measured using live atomic force microscopy (AFM) indentation, and viscoelastic parameters calculated from previously reported compression data[38] (Supplementary Fig. 1f–h). Previous analyses demonstrated that mesodermal cell polarities, division planes and movements in the axial plane are oriented towards the nearest ectoderm[4,5,10]. Therefore, mesodermal growth in the limb field was modelled as pressure normal to the under-surface of ectoderm (Supplementary Fig. 1i). Mesodermal pressure resulted in an ectodermal stress pattern that was dorsoventrally biased followed by stress relaxation due to viscoelasticity (Fig. 3a and Supplementary Video 7). This result is explained by the elongate shape of the lateral plate because focal stress in the limb field would be less easily dissipated along the short DV axis relative to the long AP axis.

To determine whether expansion of mesoderm is sufficient to polarize ectodermal actin *in vivo*, we micro-injected collagen or polyethylene glycol (PEG) hydrogel into non-limb lateral plate mesoderm to mimic limb initiation before 4 h in roller culture (Fig. 3b). Injection, but not sham needle penetration of the contralateral side, was sufficient to upregulate *Tcf/Lef::H2B–Venus* activation and to polarize cortical actin along AP cell interfaces (Fig. 3c–e). This upregulation was not associated with increased ectodermal cell proliferation (Supplementary Fig. 1j), suggesting that it was attributable to enhanced differentiation. Biased distribution of actin therefore reflects DV stress pattern and is a function of tissue geometry (Fig. 3f).

Cell division precipitates cell neighbour exchange and oriented remodelling of pre-AER ectoderm

To study dynamic relationships between neighbouring cells, we employed transgenic cell membrane reporters for live imaging. These included *CAG::myr–Venus*[35] that labelled all cells and the conditional *mT/mG* reporter[39] that permitted conversion of red to green fluorescence using *Crect*. We identified numerous tetrads and multicellular rosettes that remodel dynamically in pre-AER dorsal and ventral ectoderm (Fig. 4a,d and Supplementary Video 4). In marked contrast to *Drosophila* and other metazoa in which daughter cells maintain a shared interface most of the time[24], we found that mitosis in the mouse embryo commonly precipitated cell neighbour exchange. Immediately post-division, daughter cells severed their common interface to permit two adjacent cells to form a new interface (Fig. 4a and Supplementary Video 8). This process is similar to T1 exchange that involves four non-dividing cells in *Drosophila*[28]. A T1
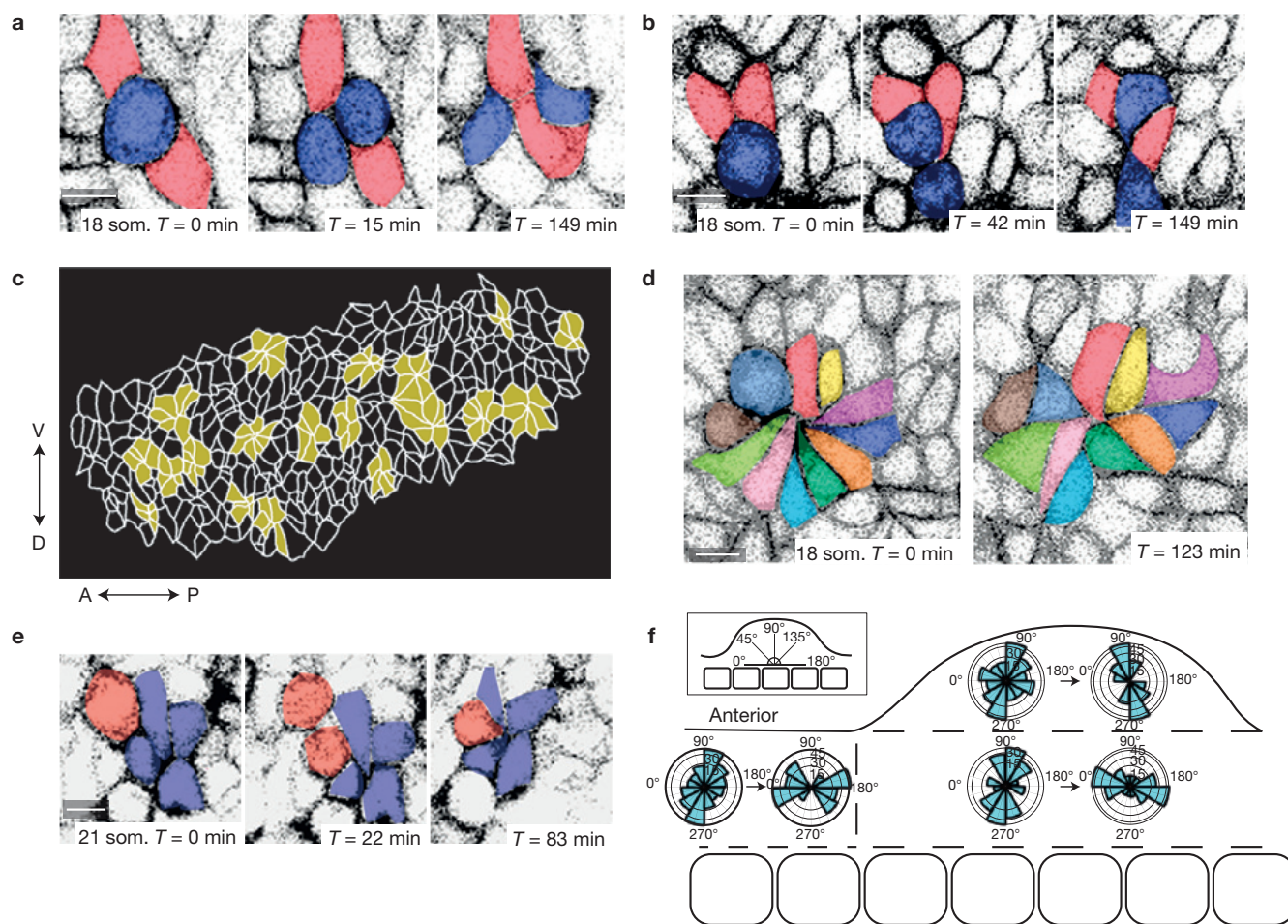
Figure 4 Cell division precipitates cell neighbour exchange and oriented remodelling of pre-AER 18–22 som. ectoderm. (**a,b**) Confocal time series of mitotic 18 som. ectodermal cells expressing *CAG::myr–Venus* demonstrates post-cell division (blue) T1-like neighbour exchange (**a**) and daughter cell intercalation among neighbours (**b**). (**c**) Outline of cell interfaces in 20 som. limb bud ectoderm with multicellular rosettes highlighted in yellow. (**d**) Time series demonstrates 18 som. rosette resolution. (**e**) The daughter cell (red) in the 18 som. limb ectoderm contributes to rosette formation following cell division. (**f**) Polar plots represent how the long axes of rosettes in different spatial regions of 18–22 som. embryos remodel during 2–3 h time-lapse videos. Long axes of rosettes are plotted at the beginning (forming or formed rosettes) and end (resolving or resolved rosettes; 49 rosettes examined, *n* = 5 embryos). Scale bars, 10 μm.

exchange alters local tissue shape by adding one cell diameter to the axis along which cells separate and subtracting one cell diameter from the orthogonal axis in which cells move together. Daughter cells also intercalated among their neighbours (Fig. 4b and Supplementary Video 9) and precipitated multicellular rosette formation (Fig. 4e and Supplementary Video 10). Rosette remodelling is analogous to T1 exchange but involves five or more cells that transiently join at a central apex[29]. Rosettes were a prominent feature as 26%–44% (18–20 som. *n* = 5 embryos) of cells were included in a rosette at a given time in both the limb field and interlimb ectoderm (Fig. 4c), and resolved through dissolution of a central apex as in *Drosophila*[29] (Fig. 4d and Supplementary Video 11). Rosettes in non-limb lateral plate and at the base of the bud resolved in a directionally biased fashion that would promote convergence of the embryo DV axis and extension of its long AP axis. In contrast, rosettes in the limb bud beyond the flank largely both formed and resolved along the PD axis (Fig. 4f). We reasoned that reorientation of rosette resolution along the PD axis of limb bud growth may be due to cell extrinsic cues.

Ectodermal tension augments DV stress pattern and orients rosettes in pre-AER limb bud

In several contexts, cell intercalations are driven by cell intrinsic forces generated by polarized actomyosin contraction[28,29,40,41]. In contrast to rosettes found in the *Drosophila* germband[29], neither actin nor myosin II (IIA, IIB, pMLC) was polarized in dorsal or ventral ectoderm beyond the zone of DV intercalation at the prospective AER despite dynamic remodelling of rosettes (Supplementary Fig. 1k). Also unlike the germband, apical/subapical actin was not polarized (Supplementary Fig. 1l). In some contexts such as the *Drosophila* wing, cell extrinsic forces drive cell rearrangements[42]. We explored whether extrinsic tissue forces might orient the stress pattern using a finite-element model of the post-initiation (22 som.) limb bud (Supplementary Fig. 1m,n). At this later stage with an established bud present, mesodermal pressure alone resulted in a relatively isotropic stress pattern and predicted bulbous tissue deformation (Fig. 5a,b and Supplementary Video 12). We then simulated AER progenitor intercalation as opposite pulling forces at the DV boundary
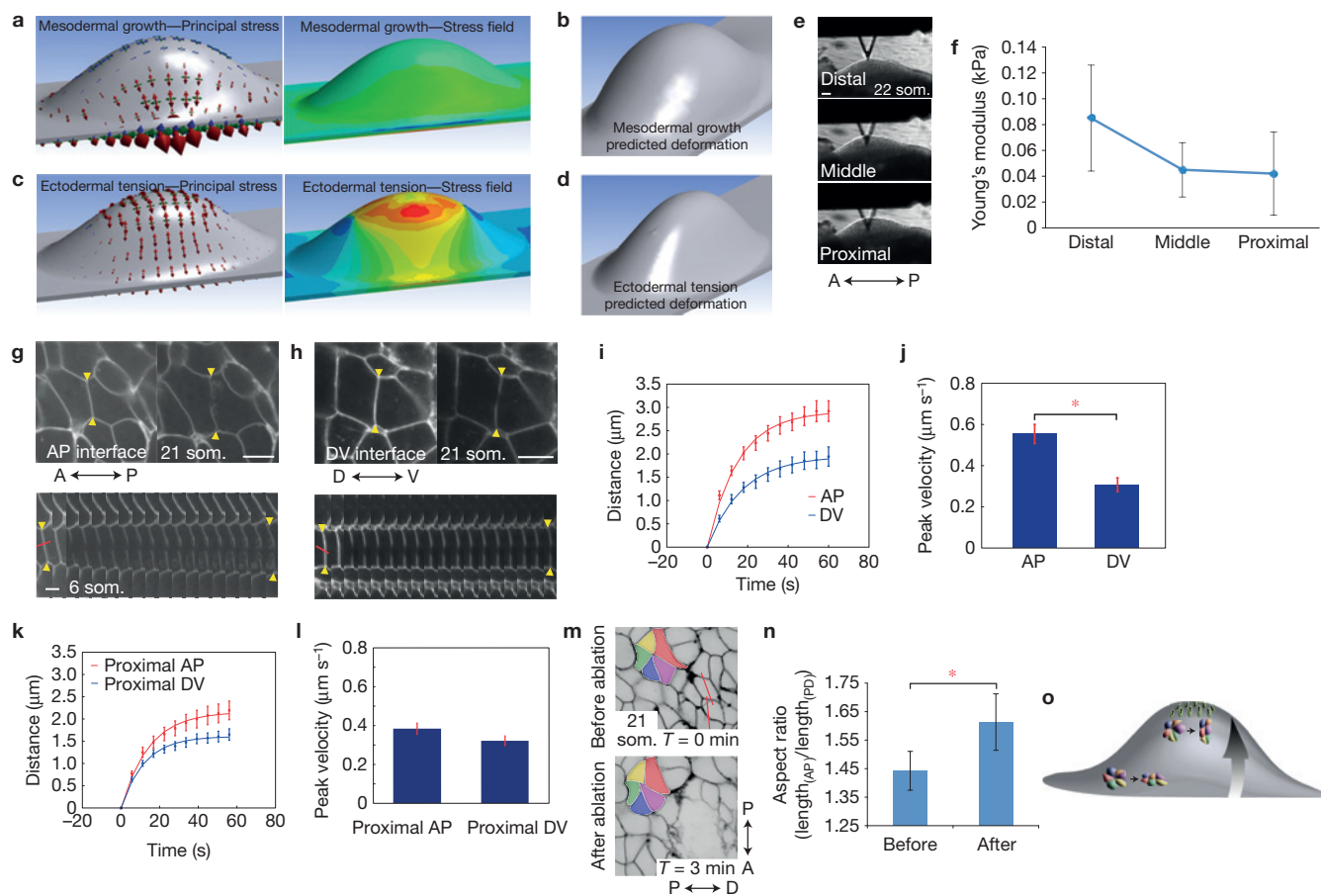
Figure 5 Tension augments the DV stress pattern and orients rosettes in pre-AER ectoderm. (**a**) Left, finite-element simulated principal stresses (red arrows) attributable to mesodermal growth alone at the 22 som. stage. Surface-plane DV:AP principal stress ratios approach 1:1. Right, simulated maximum principal stress field due to mesodermal growth. (**b**) Simulated deformation predicts bulbous tissue expansion. (**c**) Left, finite-element simulated principal stresses due to pulling forces secondary to cell intercalation at the DV boundary. Surface-plane DV:AP principal stress ratios >3:1. Right, simulated maximum principal stress field due to pulling forces at DV boundary generates tensile gradient along the PD axis. (**d**) Simulated deformation predicts maintenance of a narrow DV limb bud axis. In **a** and **c**, red, green and blue arrows indicate maximum, middle and minimum principal stresses, respectively. (**e**) AFM cantilevered tip at different PD levels. (**f**) AFM measurements of proximal, middle and distal regions of initiating limb buds were used to calculate Young's modulus ($n = 5$ embryos; $P = 0.0491$ (distal versus proximal; Student's t-test)). (**g**,**h**) Limb bud ectodermal cells expressing $R26R::mTmG$; $Crect$ before and after ablation of AP (**g**) or DV (**h**) interfaces. Lower panels,

kymographs of vertex displacement over time (6 s intervals). Yellow arrows highlight cell vertices. (**i**) Distance between two vertices adjacent to cut interface in AP and DV interfaces ($P = 0.0008$). (**j**) Peak retraction velocities of ablated AP and DV interfaces ($P = 0.0001$); (**i**,**j**) $n \sim 18$ ablations for each of eight 19–23 som. embryos. (**k**) Distance between two vertices of proximal AP or proximal DV cut interfaces ($P = 0.0442$). (**l**) Peak retraction velocities of ablated proximal AP and proximal DV interfaces ($P = 0.1208$; (**k**,**l**) $n \sim 15$ ablations for each of four 19–23 som. embryos. ((**i**–**l**) Student's t-test with Holm's correction.) (**m**) $R26R::mTmG$; $Crect$ limb bud ectoderm before and 3 min after ablation. Red lines indicate sites of ablation. (**n**) Rosette AP/PD aspect ratio ($\text{length}_{AP}/\text{length}_{PD}$) measured before and after ablation of a region distal to the rosette ($n = 6$ embryos 21–26 som.; $P = 0.019$ (Student's t-test)). (**o**) Pre-AER model. Although rosette resolution at the base of the bud occurs along the AP axis (lower rosette), intercalation of AER progenitors (green) generates a tensile gradient that redirects rosette resolution along the PD axis (top rosette). Error bars indicate s.e.m. Scale bars, $10\,\mu\text{m}$ (**g**,**h**,**m**), $100\,\mu\text{m}$ (**e**). The asterisks indicate $P < 0.01$ (**j**); $P < 0.05$ (**n**).

using piconewton values that are within the range of physiological intercellular forces measured by others[43]. This pulling force generated a dorsoventrally biased stress pattern and more realistic maintenance of a narrow DV limb bud axis (Fig. 5c,d and Supplementary Video 13; deformation analyses were used here to help validate the ectodermal stress pattern rather than to establish determinants of nuanced 3D tissue shape). We examined the effect of varying the magnitude of this pulling force twofold and found, as expected, that relative stress gradients remained linearly consistent with the magnitude of force (Supplementary Fig. 1o,p). Overall, this model suggests that a combination of mesodermal growth and ectodermal tension

theoretically generates a stress pattern that is dorsoventrally biased and of greatest magnitude at the prospective AER.

To measure the magnitude of actual ectodermal stiffness, we examined cultured mouse embryos using AFM. Young's modulus, a measure of the stiffness of an elastic material, was greatest near the distal tip at the DV midline, and diminished towards the proximal base of the bud (Fig. 5e,f). We also undertook laser ablation of individual 21–22 som. ectodermal cell interfaces. Initial recoil velocity, which is predicted to be proportional to tension[44], was substantially greater following ablation of AP interfaces near (∼5 cell diameters from) the AER relative to those near (∼5 cell diameters from) the base of the bud
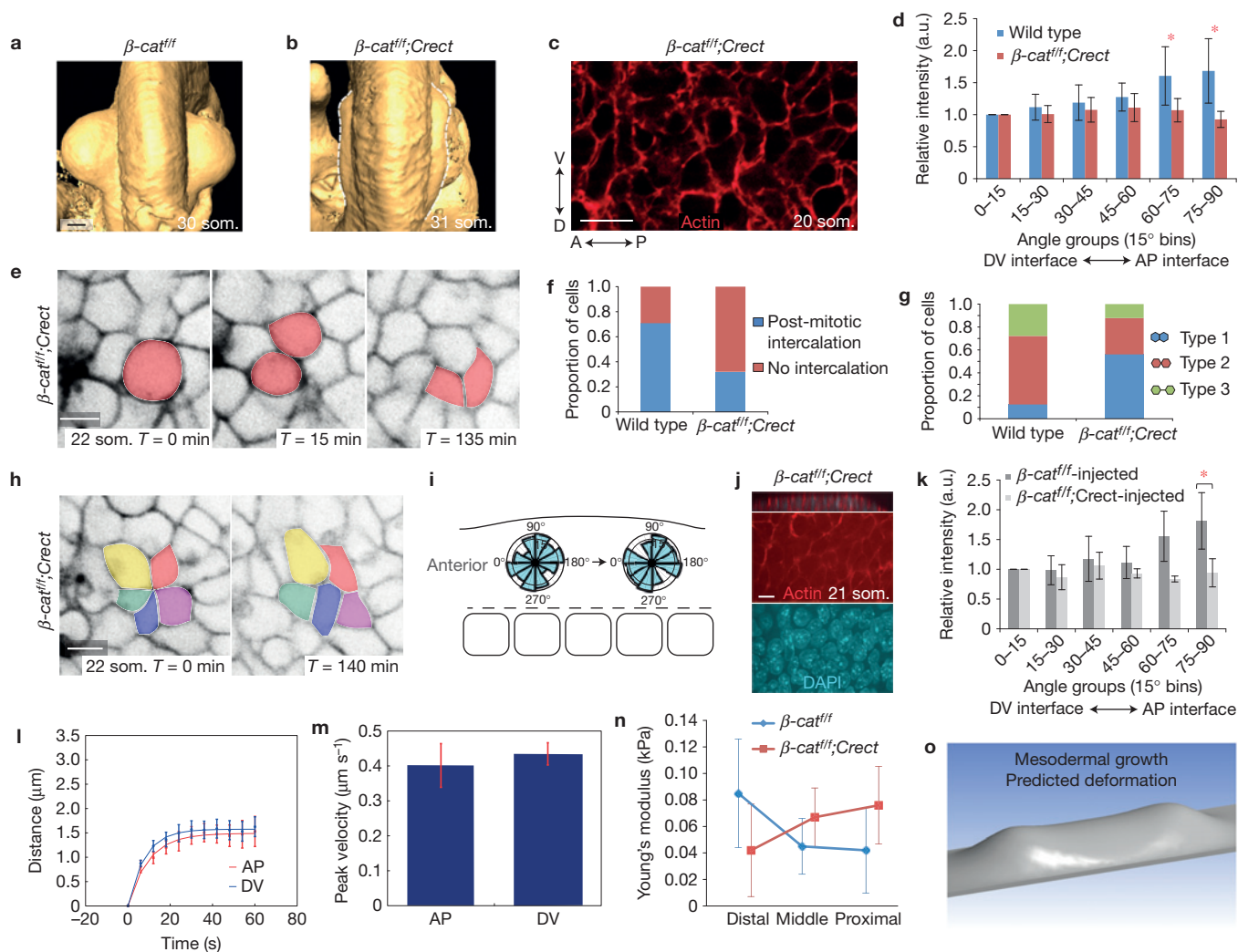
Figure 6 Ectodermal β-catenin is required to polarize actin and orient cell behaviour in response to stress. (**a,b**) Optical projection tomography of E9.75 (30–31 som.) forelimb buds in wild type (**a**) and β-cat[f/f]; Crect mutants (**b**). Dorsal views are shown; anterior is up. (**c**) Confocal image of a rhodamine–phalloidin-stained β-cat[f/f]; Crect mutant embryo showing a basal ectodermal section (compare with Fig. 2a). (**d**) Relative fluorescence intensity of actin at cell interfaces (SIESTA). Wild type n = 5 18–20 som. embryos, β-cat[f/f]; Crect n = 3 19–22 som. embryo, P = 0.0066 (60–75° bin), P = 0.0004 (75–90° bin; Student's t-test). (**e**) Time series of mitotic cells in initiating β-cat[f/f]; Crect mutant limb bud ectoderm expressing R26R::mTmG. (**f**) Proportion of daughter cells that underwent intercalation in wild-type and β-cat[f/f]; Crect mutant limb buds (P = 0.034; Student's t-test). (**g**) Proportion of Type 1, 2 and 3 interfaces[24] in wild-type and β-cat[f/f]; Crect mutant limb buds (P = 0.0042 (Student's t-test); wild type: n = 30 mitotic cells, 5 embryos; mutant: n = 25 cells, 2 embryos). Schematic representation of Type 1, 2 and 3 interfaces (right). (**h**) Confocal time series of a rosette in the central region of a β-cat[f/f]; Crect mutant limb bud ectoderm expressing R26R::mTmG. (**i**) Axes of rosette remodelling in a β-cat[f/f]; Crect mutant limb bud ectoderm (42 rosettes, n = 2 embryos). (**j**) Confocal images of collagen-injected β-cat[f/f]; Crect mutant flank ectoderm (compare with Fig. 3e). Shown are z section (top panel) and xy sections visualizing actin (red) and DAPI (blue). (**k**) Relative fluorescence intensity of actin at cell interfaces (SIESTA; n = 3 19–21 som. embryos per condition, P = 0.0046 75–90° bin mutant versus control (Student's t-test)). (**l**) Distance between two vertices attached to either AP or DV cut interfaces in β-cat[f/f]; Crect mutant limb bud ectoderm (P = 0.43). (**m**) Peak retraction velocities of ablated AP and DV interfaces in β-cat[f/f]; Crect mutant limb bud ectoderm (P = 0.36; (**l,m**) n ~ 15 ablations over four 21–25 som. embryos for each condition (Student's t-test with Holm's correction)). (**n**) AFM measurements of proximal, middle and distal regions of initiating wild-type and β-cat[f/f]; Crect mutant limb buds were used to calculate Young's modulus (n = 5 control embryos, n = 3 mutant embryos; P = 0.0435 (distal control versus mutant; Student's t-test)). (**o**) Simulated deformation of an early bud based on mutant Young's modulus of 0.042 kPa (compare with Fig. 5b). Scale bars, 10 µm (**c,e,h,j**), 200 µm (**a,b**). Error bars indicate s.e.m. Asterisk indicates P < 0.05.

(Supplementary Fig. 1q,r). These data suggest that a tensile gradient emanates from the prospective AER.

To determine directionality of ectodermal tension, we compared retraction velocities of orthogonal interfaces in different locations. Near the prospective AER, ablated AP interfaces retracted substantially faster than those of DV interfaces (Fig. 5g–j and

Supplementary Videos 14 and 15), indicating the presence of anisotropic tension. Consistent with spatial differences that we had observed in axes of resolving rosettes, anisotropy was diminished near the base of the bud and in non-limb lateral plate ectoderm (Fig. 5k,l and Supplementary Fig. 1s,t). Tension that we measured using laser ablation was ~1.4-fold different along the PD axis (Fig. 5j,l and
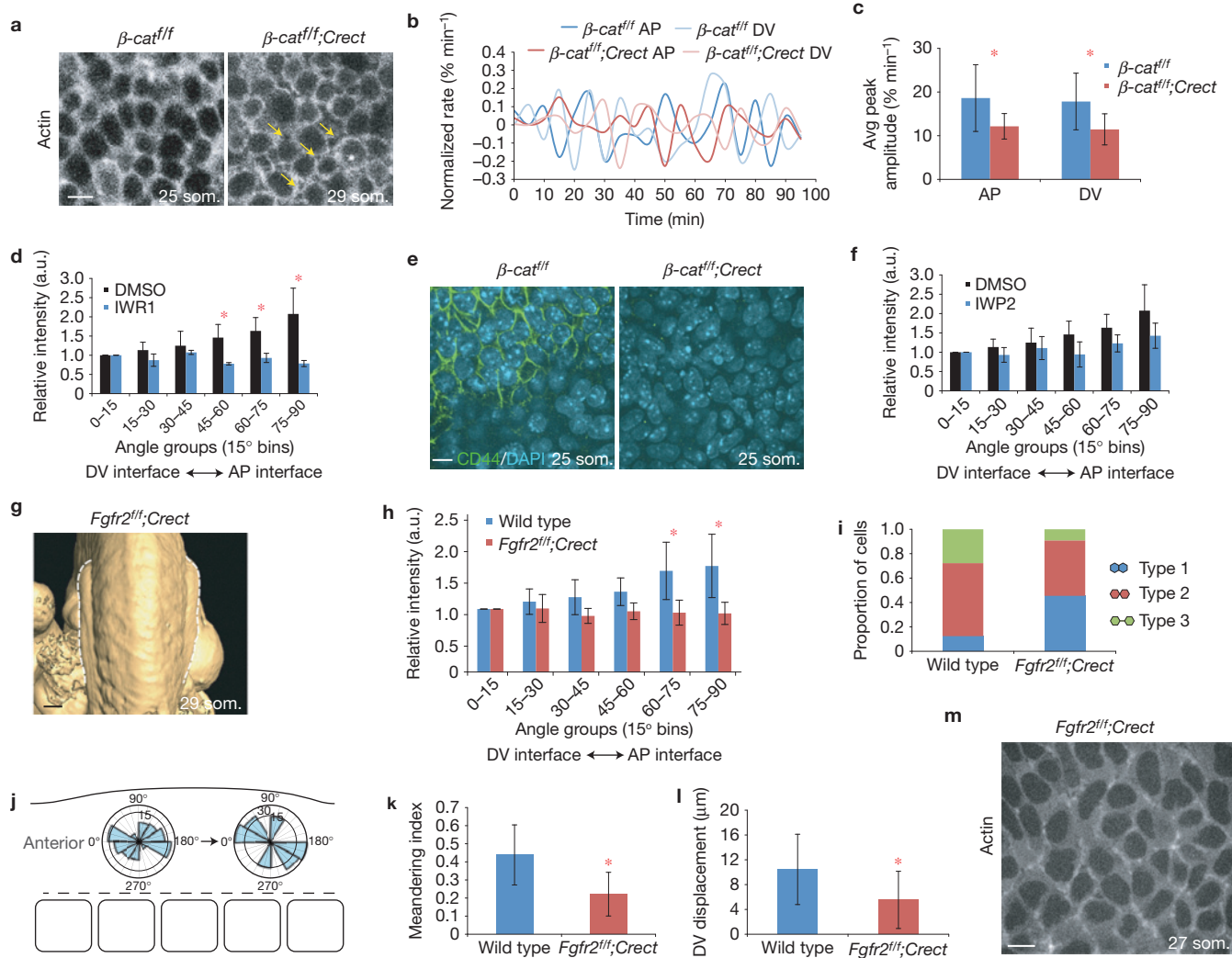
Figure 7 Direct and indirect functions of β-catenin and Fgfr2. (**a**) Confocal images of control $β\text{-}cat^{f/f}$ and $β\text{-}cat^{f/f}$; Crect mutant limb bud ectoderm at the 25 and 29 som. stage expressing $R26R::Venus\text{-}actin$. Yellow arrows indicate sites of cortical separation. (**b**) Rate of change of interface length from time-lapse videos of control and $β\text{-}cat^{f/f}$; Crect mutant limb bud ectoderm expressing $R26R::Venus\text{-}actin$, normalized to maximum interface length. Shown are representative curves from 4 interfaces. (**c**) Peak amplitude of oscillation of AP and DV interfaces in control $β\text{-}cat^{f/f}$ and $β\text{-}cat^{f/f}$; Crect mutant limb bud ectoderm ($n = 32$ interfaces for each condition; $P = 4.2 \times 10^{-5}$ (AP) $P = 1.0 \times 10^{-5}$ (DV; Student's t-test). (**d**) Relative fluorescence intensity of actin at cell interfaces in limb bud ectoderm of embryos that were treated with IWR-1 or vehicle control (dimethylsulphoxide (DMSO)) for 6 h was quantified using SIESTA software and plotted over 90° ($n = 3$ 19–22 som. embryos per condition; $P = 0.0031$ (45–60° bin), $P = 0.035$ (60–75° bin), $P = 0.015$ (75–90° bin) (Student's t-test). (**e**) Confocal images of control $β\text{-}cat^{f/f}$ and $β\text{-}cat^{f/f}$; Crect mutant ectoderm visualizing CD44 (green) and DAPI (blue). (**f**) Relative fluorescence intensity of actin at cell interfaces of embryos treated with IWP-2 or vehicle control (DMSO) for 6 h (SIESTA; $n = 3$ 19–22 som.

embryos per condition; $P = 0.31$ (75–90° bin) (Student's t-test). (**g**) Optical projection tomography image of E9.75 $Fgfr2^{f/f}$; Crect mutant forelimbs. Dorsal views, anterior up. (**h**) Relative fluorescence intensity of actin at cell interfaces (SIESTA; wild type $n = 5$ embryos, $Fgfr2^{f/f}$; Crect $n = 3$, $P = 0.00015$ (60–75° bin), $P = 4.2 \times 10^{-5}$ (75–90° bin), (Student's t-test). (**i**) Proportion of Type 1, 2 and 3 interfaces[24] in wild-type and $Fgfr2^{f/f}$; Crect mutant limb buds ($P = 0.093$ (Student's t-test); wild type: $n = 30$ mitotic cells, 5 embryos; mutant: $n = 11$ cells, 3 embryos). (**j**) Axes of rosette remodelling in $Fgfr2^{f/f}$; Crect mutant limb bud ectoderm (20 rosettes, $n = 2$ embryos). (**k**) Meandering index (displacement/total distance travelled) of Tcf-positive nuclei near the DV boundary of wild-type and $Fgfr2^{f/f}$; Crect mutant limb buds, $P = 3.5 \times 10^{-4}$ (Student's t-test). (**l**) DV displacement of Tcf-positive nuclei near the DV boundary of wild-type and $Fgfr2^{f/f}$; Crect mutant limb buds, $P = 0.02$ (Student's t-test). (For **k** and **l**, $n = 20$ cells over 2 h in three 21–25 som., embryos for each.) (**m**) $Fgfr2^{f/f}$; Crect mutant limb bud ectoderm expressing $R26R::Venus\text{-}actin$. Scale bars, 10 μm (**a**,**e**,**m**), 200 μm (**g**). Error bars indicate s.e.m. Asterisk indicates $P < 0.05$ (**d**,**h**,**l**) and $P < 0.01$ (**c**,**k**).

Supplementary Fig. 1r), whereas finite-element simulation predicted a difference of ∼1.5–1.55-fold (Supplementary Fig. 1o,p). This difference may exist in part because the model does not incorporate viscoelastic effects of cell rearrangements.

To determine whether DV tension emanates from the prospective AER, we disrupted 3–5 cell interfaces in a linear fashion parallel to

the prospective AER. This procedure diminished retraction velocities of single AP interfaces proximal to the disruption (Supplementary Fig. 1u,v). We used linear ablation also to examine whether tension is necessary to orient rosette resolution. Immediately following ablation, PD long axes of rosettes proximal to the ablation were shortened, suggesting that distally based tension was resisting rosette contraction.

Also, whereas rosettes in the limb bud normally resolved along the PD axis (Fig. 4f), ablation resulted in resolution along the orthogonal (AP) axis (Fig. 5m,n and Supplementary Video 16). Therefore, distally biased tension is necessary to orient rosette resolution along the axis of limb bud growth (Fig. 5o).

Ectodermal β-catenin is required to polarize actin and orient cell behaviour in response to stress

Unexpectedly, most single and compound planar cell polarity (PCP) pathway mouse mutants do not lack an AER nor exhibit marked early limb bud phenotypes despite convergent extension defects of the long embryo axis and of other organ systems[5,6,45–47]. Consistent with mutant data, select markers of PCP such as Frizzled 6 and Dishevelled 3, and apical–basal polarity markers Par-1 and Par-3 were not polarized among ectodermal cells (Supplementary Fig. 2a,d). We also examined zebrafish PCP mutants that exhibit marked shortening of their body axis secondary to convergent-extension defects. Neither maternal-zygotic *Vangl2* (*trilobite*)[48], nor *Wnt5* (*pipetail*)[49], nor *atypical protein kinase C* (*heart and soul*)[50] mutants exhibited gross pectoral fin anomalies (Supplementary Fig. 2e–k). Therefore, as for the *Drosophila* germband[51], evidence that early limb bud morphogenesis is regulated by the PCP pathway is lacking, although it is possibly masked by redundancy.

To investigate the function of the canonical Wnt pathway in ectoderm, we conditionally deleted *β-catenin* using *Crect*, which is activated before limb initiation (Supplementary Fig. 3a). In conditional mutants, affected embryos survived to at least E18.5 and, although the limb bud initiated, it failed to progress beyond a shallow saddle shape that lacked an AER (Fig. 6a,b) and did not develop skeletal elements beyond the scapula and pelvis (Supplementary Fig. 3b). As expected, conditional mutants exhibited ectoderm-specific loss of membrane-associated β-catenin (Supplementary Fig. 3c) and marked reduction of ectodermal *Tcf/Lef::H2B–Venus* reporter activity (Supplementary Fig. 3d,e). Proliferation and apoptosis were not affected in either ectoderm or mesoderm at the pre-AER, 22 som. stage (Supplementary Fig. 3f–j). Moreover, mesodermal expression of *Fgf10* was maintained in 22 som. mutant limb buds despite the presence of a clear phenotype in mutants (Supplementary Fig. 3k). *Fgf10* expression was attenuated at a later stage when its expression presumably becomes dependent on ectodermal feedback[14] (Supplementary Fig. 3l). These data suggest that the early (22 som. E9.25) mutant phenotype we observed (Supplementary Fig. 3k) was not obviously attributable to failure of mesodermal growth although mesodermal apoptosis at a later stage (35 som.) has been associated with a similar limb bud phenotype[10]. An alternate possibility was that organized cell behaviours were compromised.

In conditional *β-catenin* mutants, cell elongation was diminished (Supplementary Fig. 4a,b), distribution of cortical actin was not biased (Fig. 6c,d), and DV intercalation of midline cells did not occur (Supplementary Fig. 4c). Daughter cell neighbour exchange events were less frequent (Fig. 6e,f and Supplementary Video 17), and the proportion of daughter cells that retained a common interface increased fivefold (Fig. 6g), more closely resembling that of other metazoa[24]. Rosettes were still present in mutants, but were oriented randomly (Fig. 6h,i and Supplementary Video 18). We examined whether the canonical Wnt pathway is required to polarize actin in response to physical stress. Injection of the same volume of collagen

generated a similar bulge in conditional *β-catenin* mutants as in wild-type embryos, but failed to polarize actin (Fig. 6j,k). These findings suggest that β-catenin is required to transduce stress as shown in other contexts[52].

Laser ablation in conditional *β-catenin* mutants revealed that ectodermal stress was no longer directionally biased in the absence of *β-catenin* (Fig. 6l,m) and a distal-high to proximal-low tensile gradient was lacking by AFM (Fig. 6n and Supplementary Fig. 4d,e). Interestingly, deformation analysis using Young's modulus measured from *β-catenin* mutant ectoderm (0.042 kPa) predicted a peculiar saddle shape that is qualitatively similar to the actual shape of conditional *β-catenin* mutants (Fig. 6o, compare with 6b). Despite being oversimplified, this simulation suggests that a key function of β-catenin is to help establish anisotropic mechanical tissue properties.

Direct and indirect functions of β-catenin and Fgfr2

Transmission of force between cells requires cell–cell adhesion, cortical tension and cortex-to-membrane attachment[53]. Despite loss of membrane-associated β-catenin, E-cadherin, a key mediator of cell–cell adhesion, was present at the cell membrane in conditional *β-catenin* mutants (Supplementary Fig. 4f). To examine cortical function, we activated *R26R:Venus–actin*[32] in ectoderm using *Crect*. We expected this reporter to label relatively recently polymerized actin in 20 som. stage embryos because *Crect* is activated robustly just before the 17 som. stage (~E9.0; Supplementary Fig. 3a). Unlike the continuous meshwork of cortical actin in wild-type ectoderm, conditional *β-catenin* mutants exhibited distinct rings of actin with intervening gaps that suggested cortices were separated from membranes and cortices between cells were uncoupled (Fig. 7a). Cortical ring morphology was reflected by a diminished number of vertices (cell 'corners' that are visibly shared with neighbouring cells) among *β-catenin* mutant cells (0.40 ± 0.025 (s.e.m.), $n = 2$) relative to wild-type cells (2.31 ± 0.075 (s.e.m.); $P = 0.0017$, $n = 2$). Consistent with cortex–membrane separation, oscillatory cell interface contractions[30] exhibited a diminished rate of change and dampened amplitude in conditional *β-catenin* mutants (Fig. 7b,c and Supplementary Videos 19 and 20). Therefore, β-catenin mechanically couples cells by promoting cortex to membrane attachment, a function that is attributable to its well-recognized role in linking the cytoskeleton to E-cadherin[52].

β-catenin might also help to polarize actin distribution indirectly through transcriptional regulation. To examine whether acute inactivation of the canonical Wnt pathway affects ectodermal cell polarity, we treated mouse embryos in roller culture with IWR1, which stabilizes the β-catenin destruction complex[54]. This inhibitor downregulated expression of *Axin2* (Supplementary Fig. 4g) and abolished polarized distribution of actin following 6 h (Fig. 7d), but not 2 h (Supplementary Fig. 4h) of treatment, suggesting that an indirect mechanism is required to maintain actin polarity. Consistent with a transcriptional role, we found that expression of CD44, a transmembrane protein that marks the AER (ref. 55) and is downstream of the canonical Wnt pathway[56], was lost in *β-catenin* conditional mutants (Fig. 7e). Loss of CD44 expression in ventral pre-AER ectoderm suggests that AER progenitors lost or never acquired appropriate identity, and represents an additional potential cause of cortical separation. We then treated embryos with

IWP2, a pan-Wnt ligand secretion inhibitor[54]. Actin polarity was not significantly affected despite diminished Dishevelled protein phosphorylation (Fig. 7f and Supplementary Fig. 4h), suggesting that stress-related Tcf/Lef activation is ligand-independent. These findings suggest that at least some transcriptional functions of β-catenin may contribute to ectodermal remodelling.

As Fgfr2 participates in a feedback loop together with the canonical Wnt pathway in ectoderm[11], we conditionally deleted floxed *Fgfr2*[57] from ectoderm using *Crect*. The most important distinguishing feature of conditional *Fgfr2* mutants was that they retained membrane-associated β-catenin (Supplementary Fig. 5a) despite partial reduction of *Tcf/Lef::H2B–Venus* reporter activity (Supplementary Fig. 5b). As expected, phospho-(p) ERK, an indicator of Fgf signalling, was markedly diminished in ectoderm (Supplementary Fig. 5c). Like conditional *β-catenin* mutants, conditional *Fgfr2* mutant buds exhibited a shallow saddle shape that failed to progress (Fig. 7g and Supplementary Fig. 5d) despite normal proliferation and apoptosis in ectoderm and mesoderm (Supplementary Fig. 5e–h), intact E-cadherin (Supplementary Fig. 5i), and mesodermal Fgf10 expression at pre-AER stages (Supplementary Fig. 5j). DV cell elongation was diminished (Supplementary Fig. 5k,l), actin was not polarized at limb initiation (Fig. 7h) and cells did not accumulate at the DV boundary (Supplementary Fig. 5m). Expression of CD44, which is also downstream of the Fgf pathway[58], was lost (Supplementary Fig. 5n). Phosphorylation of β-catenin Tyr 654 that is associated with reduced association of β-catenin with E-cadherin[59] was not enhanced in conditional *Fgfr2* mutants (Supplementary Fig. 5o). This finding supports the concept that ectodermal functions of Fgfr2 were largely independent of membrane-associated β-catenin at early limb bud stages. Of course, it is possible that β-catenin and Fgfr2 pathways are acting entirely by influencing junctional proteins, although some of these may be indirect targets. CD44, for example, promotes migratory cell behaviour by presenting Fgf to neighbouring cells and links the extracellular environment to the cytoskeleton[55]. Overall, *Fgfr2* mutant embryos exhibited many of the same features as conditional *β-catenin* mutants, findings that support their function in a common pathway.

However, some cell neighbour exchange events were subtly distinct in conditional *Fgfr2* mutants. Daughter cells shared a long interface less frequently than in *β-catenin* mutants, and rosettes exhibited a greater degree of orientation along the AP axis although they did not effectively reorient along the DV axis (Fig. 7i,j, compare with 6g,i). *Tcf/Lef::H2B–Venus*-positive cells were also relatively mobile in conditional *Fgfr2* mutants (Supplementary Video 21) but meandered to a greater extent than wild-type cells (Fig. 7k,l) and failed to accumulate in the prospective AER (Supplementary Fig. 5m). We propose that intact membrane-associated β-catenin and persistent cortical attachment in *Fgfr2* mutants (Fig. 7m) underlies this improved ability to undertake neighbour exchange in comparison to *β-catenin* mutants.

DISCUSSION

It has been suggested that integration of local forces generated by cells into a global force pattern feeds back to individual cells to refine their behaviour and determine ultimate tissue shape[2]. Our findings substantiate this concept by showing that initial mesodermal growth anisotropically stresses ectoderm as a function of tissue geometry, thereby polarizing ectodermal cells along the DV axis. Intercalation

of those cells at the DV boundary generates further tension in the ectodermal plane that reorients rosette resolution near the prospective AER. Therefore, mesoderm and ectoderm cooperatively generate a stress pattern that is mediated by β-catenin and Fgfr2 to orient ectodermal cell rearrangements.

It has been postulated that AER position might be defined by a border of ectodermal BMP activity because both loss and gain of BMP function results in failure of AER formation[7,12,13] or by apposition of pre-specified dorsal and ventral ectodermal compartments[7], although AER formation can be dissociated from DV polarity[20]. A related possibility raised by our findings is that ectodermal sheets that are polarized to remodel along the DV axis gradually deliver a subset of cells (definitive AER progenitors) to the DV boundary owing to physical constraints. This process is reminiscent of 'convergent thickening' as described for *Xenopus* blastopore closure[60].

Mouse ectoderm exhibits some cell behaviours that are divergent with respect to those of invertebrates and other vertebrates[24]. For tissues in which rapid cell division and rearrangement are concomitant, daughter cell intercalation may increase tissue fluidity to dissipate energy and facilitate orderly tissue shape change. Rosette remodelling facilitates directional tissue shape change[29,36,61] and buffers disequilibrium during morphogenetic movements[62]. Evidence here supports the concept that rosette formation is facilitated, in part, by cell-intrinsic planar-polarized actin and protrusive activity. Following cell division, rosette formation may buffer transient cell packing disequilibrium in mouse ectoderm. The axis of rosette resolution, on the other hand, is oriented by cell extrinsic stress. By improving the resolution with which we can quantify physical parameters during development, we will refine models of how cell behaviours generate embryonic shapes. □

METHODS

Methods and any associated references are available in the online version of the paper.

Note: Supplementary Information is available in the online version of the paper

AUTHOR CONTRIBUTIONS
K.L., H.T. and S.H. designed the experiments. H.T., H.L., C.S. and Y.S. performed and analysed AFM experiments. J.W. performed FEM. K.L., H.T., K.S. and S.H. performed and analysed live imaging and immunofluorescence experiments. N.S. performed cell neighbour analysis. K.L., K.S., S.L., J.T.A.B. and I.S. performed and analysed injection experiments. M.D.W. and R.M.H. performed OPT experiments. D.L. analysed cell division plane and rosette remodelling data. S.D. performed measurements of lateral plate ectoderm. S.H. and B.C. performed zebrafish experiments. T.W. provided Crect mice. A-K.H. provided CAG::myr–Venus and Tcf/Lef::H2B–Venus mice. K.L. and R-F-G. performed and analysed laser ablation experiments. R-F-G. provided SIESTA software and MATLAB scripts. S.H. wrote the manuscript.

1. Keller, R. Developmental biology. Physical biology returns to morphogenesis. *Science* **338**, 201–203 (2012).

2. Heisenberg, C. P. & Bellaiche, Y. Forces in tissue morphogenesis and patterning. *Cell* **153,** 948–962 (2013).
3. Hopyan, S., Sharpe, J. & Yang, Y. Budding behaviors: growth of the limb as a model of morphogenesis. *Dev. Dyn.* **240,** 1054–1062 (2011).
4. Boehm, B. *et al.* The role of spatially controlled cell proliferation in limb bud morphogenesis. *PLoS Biol.* **8,** e1000420 (2010).
5. Gros, J. *et al.* WNT5A/JNK and FGF/MAPK pathways regulate the cellular events shaping the vertebrate limb bud. *Curr. Biol.* **20,** 1993–2002 (2010).
6. Wyngaarden, L. A. *et al.* Oriented cell motility and division underlie early limb bud morphogenesis. *Development* **137,** 2551–2558 (2010).
7. Fernandez-Teran, M. & Ros, M. A. The apical ectodermal ridge: morphological aspects and signaling pathways. *Int. J. Dev. Biol.* **52,** 857–871 (2008).
8. Heintzelman, K. F., Phillips, H. M. & Davis, G. S. Liquid-tissue behavior and differential cohesiveness during chick limb budding. *J. Embryol. Exp. Morphol.* **47,** 1–15 (1978).
9. Hornbruch, A. & Wolpert, L. Cell division in the early growth and morphogenesis of the chick limb. *Nature* **226,** 764–766 (1970).
10. Barrow, J. R. *et al.* Ectodermal Wnt3/β-catenin signaling is required for the establishment and maintenance of the apical ectodermal ridge. *Genes Dev.* **17,** 394–409 (2003).
11. Kawakami, Y. *et al.* WNT signals control FGF-dependent limb initiation and AER induction in the chick embryo. *Cell* **104,** 891–900 (2001).
12. Pizette, S., Abate-Shen, C. & Niswander, L. BMP controls proximodistal outgrowth, via induction of the apical ectodermal ridge, and dorsoventral patterning in the vertebrate limb. *Development* **128,** 4463–4474 (2001).
13. Soshnikova, N. *et al.* Genetic interaction between Wnt/β-catenin and BMP receptor signaling during formation of the AER and the dorsal-ventral axis in the limb. *Genes Dev.* **17,** 1963–1968 (2003).
14. Xu, X. *et al.* Fibroblast growth factor receptor 2 (FGFR2)-mediated reciprocal regulation loop between FGF8 and FGF10 is essential for limb induction. *Development* **125,** 753–765 (1998).
15. Ibrahimi, O. A., Chiu, E. S., McCarthy, J. G. & Mohammadi, M. Understanding the molecular basis of Apert syndrome. *Plast. Reconstr. Surg.* **115,** 264–270 (2005).
16. Niemann, S. *et al.* Homozygous WNT3 mutation causes tetra-amelia in a large consanguineous family. *Am. J. Hum. Genet.* **74,** 558–563 (2004).
17. Bell, S. M., Schreiner, C. M. & Scott, W. J. The loss of ventral ectoderm identity correlates with the inability to form an AER in the legless hindlimb bud. *Mech. Dev.* **74,** 41–50 (1998).
18. Altabef, M. & Tickle, C. Initiation of dorso-ventral axis during chick limb development. *Mech. Dev.* **116,** 19–27 (2002).
19. Guo, Q., Loomis, C. & Joyner, A. L. Fate map of mouse ventral limb ectoderm and the apical ectodermal ridge. *Dev. Biol.* **264,** 166–178 (2003).
20. Loomis, C. A., Kimmel, R. A., Tong, C. X., Michaud, J. & Joyner, A. L. Analysis of the genetic pathway leading to formation of ectopic apical ectodermal ridges in mouse Engrailed-1 mutant limbs. *Development* **125,** 1137–1148 (1998).
21. Milaire, J. [La morphogenese des membres]. *Bull. Acad. R. Med. Belg.* **129,** 341–361 (1974).
22. Altabef, M., Clarke, J. D. & Tickle, C. Dorso-ventral ectodermal compartments and origin of apical ectodermal ridge in developing chick limb. *Development* **124,** 4547–4556 (1997).
23. Zallen, J. A. & Zallen, R. Cell-pattern disordering during convergent extension in *Drosophila. J. Phys. Condens. Matter* **16,** S5073–S5080 (2004).
24. Gibson, M. C., Patel, A. B., Nagpal, R. & Perrimon, N. The emergence of geometric order in proliferating metazoan epithelia. *Nature* **442,** 1038–1041 (2006).
25. Hadjantonakis, A. K. & Papaioannou, V. E. Dynamic *in vivo* imaging and cell tracking using a histone fluorescent protein fusion in mice. *BMC Biotechnol.* **4,** 33 (2004).
26. Ferrer-Vaquer, A. *et al.* A sensitive and bright single-cell resolution live imaging reporter of Wnt/ss-catenin signaling in the mouse. *BMC Dev. Biol.* **10,** 121 (2011).
27. Larsen, M., Wei, C. & Yamada, K. M. Cell and fibronectin dynamics during branching morphogenesis. *J. Cell Sci.* **119,** 3376–3384 (2006).
28. Bertet, C., Sulak, L. & Lecuit, T. Myosin-dependent junction remodelling controls planar cell intercalation and axis elongation. *Nature* **429,** 667–671 (2004).
29. Blankenship, J. T., Backovic, S. T., Sanny, J. S., Weitz, O. & Zallen, J. A. Multicellular rosette formation links planar cell polarity to tissue morphogenesis. *Dev. Cell* **11,** 459–470 (2006).
30. Fernandez-Gonzalez, R. & Zallen, J. A. Oscillatory behaviors and hierarchical assembly of contractile structures in intercalating cells. *Phys. Biol.* **8,** 045005 (2011).
31. Gao, Y., Dickerson, J. B., Guo, F., Zheng, J. & Zheng, Y. Rational design and characterization of a Rac GTPase-specific small molecule inhibitor. *Proc. Natl Acad. Sci. USA* **101,** 7618–7623 (2004).
32. Abe, T. *et al.* Establishment of conditional reporter mouse lines at ROSA26 locus for live cell imaging. *Genesis* **49,** 579–590 (2011).
33. Reid, B. S., Yang, H., Melvin, V. S., Taketo, M. M. & Williams, T. Ectodermal Wnt/β-catenin signaling shapes the mouse face. *Dev. Biol.* **349,** 261–269 (2011).
34. Shih, J. & Keller, R. Cell motility driving mediolateral intercalation in explants of Xenopus laevis. *Development* **116,** 901–914 (1992).
35. Rhee, J. M. *et al. In vivo* imaging and differential localization of lipid-modified GFP-variant fusions in embryonic stem cells and mice. *Genesis* **44,** 202–218 (2006).
36. Williams, M., Yen, W., Lu, X. & Sutherland, A. Distinct apical and basolateral mechanisms drive planar cell polarity-dependent convergent extension of the mouse neural plate. *Dev. Cell* **29,** 34–46 (2014).
37. Galkin, V. E., Orlova, A. & Egelman, E. H. Actin filaments as tension sensors. *Curr. Biol.* **22,** R96–101 (2012).
38. Forgacs, G., Foty, R. A., Shafrir, Y. & Steinberg, M. S. Viscoelastic properties of living embryonic tissues: a quantitative study. *Biophys. J.* **74,** 2227–2234 (1998).
39. Muzumdar, M. D., Tasic, B., Miyamichi, K., Li, L. & Luo, L. A global double-fluorescent Cre reporter mouse. *Genesis* **45,** 593–605 (2007).
40. Bosveld, F. *et al.* Mechanical control of morphogenesis by Fat/Dachsous/Four-jointed planar cell polarity pathway. *Science* **336,** 724–727 (2012).
41. Shindo, A. & Wallingford, J. B. PCP and septins compartmentalize cortical actomyosin to direct collective cell movement. *Science* **343,** 649–652 (2014).
42. Aigouy, B. *et al.* Cell flow reorients the axis of planar polarity in the wing epithelium of *Drosophila. Cell* **142,** 773–786 (2010).
43. Borghi, N. *et al.* E-cadherin is under constitutive actomyosin-generated tension that is increased at cell–cell contacts upon externally applied stretch. *Proc. Natl Acad. Sci. USA* **109,** 12568–12573 (2012).
44. Hutson, M. S. *et al.* Forces for morphogenesis investigated with laser microsurgery and quantitative modeling. *Science* **300,** 145–149 (2003).
45. Gao, B. *et al.* Wnt morphogen gradients establish planar cell polarity by inducing Vangl2 phosphorylation through Ror2. *Dev. Cell* **20,** 163–176 (2011).
46. Wang, Y., Guo, N. & Nathans, J. The role of Frizzled3 and Frizzled6 in neural tube closure and in the planar polarity of inner-ear sensory hair cells. *J. Neurosci.* **26,** 2147–2156 (2006).
47. Saburi, S. *et al.* Loss of Fat4 disrupts PCP signaling and oriented cell division and leads to cystic kidney disease. *Nat. Genet.* **40,** 1010–1015 (2008).
48. Ciruna, B., Jenny, A., Lee, D., Mlodzik, M. & Schier, A. F. Planar cell polarity signalling couples cell division and morphogenesis during neurulation. *Nature* **439,** 220–224 (2006).
49. Kilian, B. *et al.* The role of Ppt/Wnt5 in regulating cell shape and movement during zebrafish gastrulation. *Mech. Dev.* **120,** 467–476 (2003).
50. Horne-Badovinac, S. *et al.* Positional cloning of heart and soul reveals multiple roles for PKC lambda in zebrafish organogenesis. *Curr. Biol.* **11,** 1492–1502 (2001).
51. Zallen, J. A. & Wieschaus, E. Patterned gene expression directs bipolar planar polarity in *Drosophila. Dev. Cell* **6,** 343–355 (2004).
52. Huveneers, S. & de Rooij, J. Mechanosensitive systems at the cadherin-F-actin interface. *J. Cell Sci.* **126,** 403–413 (2013).
53. Maitre, J. L. *et al.* Adhesion functions in cell sorting by mechanically coupling the cortices of adhering cells. *Science* **338,** 253–256 (2012).
54. Chen, B. *et al.* Small molecule-mediated disruption of Wnt-dependent signaling in tissue regeneration and cancer. *Nat. Chem. Biol.* **5,** 100–107 (2009).
55. Sherman, L., Wainwright, D., Ponta, H. & Herrlich, P. A splice variant of CD44 expressed in the apical ectodermal ridge presents fibroblast growth factors to limb mesenchyme and is required for limb outgrowth. *Genes Dev.* **12,** 1058–1071 (1998).
56. Wielenga, V. J. *et al.* Expression of CD44 in Apc and Tcf mutant mice implies regulation by the WNT pathway. *Am. J. Pathol.* **154,** 515–523 (1999).
57. Yu, K. *et al.* Conditional inactivation of FGF receptor 2 reveals an essential role for FGF signaling in the regulation of osteoblast function and bone growth. *Development* **130,** 3063–3074 (2003).
58. Shimabukuro, Y. *et al.* Fibroblast growth factor-2 stimulates directed migration of periodontal ligament cells via PI3K/AKT signaling and CD44/hyaluronan interaction. *J. Cell Physiol.* **226,** 809–821 (2011).
59. Roura, S., Miravet, S., Piedra, J., Garcia de Herreros, A. & Dunach, M. Regulation of E-cadherin/Catenin association by tyrosine phosphorylation. *J. Biol. Chem.* **274,** 36734–36740 (1999).
60. Keller, R. & Danilchik, M. Regional expression, pattern and timing of convergence and extension during gastrulation of Xenopus laevis. *Development* **103,** 193–209 (1988).
61. Lienkamp, S. S. *et al.* Vertebrate kidney tubules elongate using a planar cell polarity-dependent, rosette-based mechanism of convergent extension. *Nat. Genet.* **44,** 1382–1387 (2012).
62. Trichas, G. *et al.* Multi-cellular rosettes in the mouse visceral endoderm facilitate the ordered migration of anterior visceral endoderm cells. *PLoS Biol.* **10,** e1001256 (2012).

METHODS

Live imaging. Live image acquisition was performed as described previously[6]. Briefly, embryos were submerged in 50% rat serum in DMEM (Invitrogen) in a 25 mm imaging chamber. Cheese cloth was used to immobilize the embryo and position the initiating limb bud directly against the coverglass. Embryos were imaged in a humidified chamber at 37 °C in 5% CO_2. Time-lapse images were acquired on a Zeiss LSM510 META confocal microscope at ×20 or ×40 magnification or a Quorum spinning-disc confocal microscope at ×20 magnification. Images were processed with Volocity software or ImageJ. Representative images are shown from at least 3 independent experiments for each condition, and unless otherwise indicated, from at least 3 independent cohorts. No statistical method was used to predetermine sample size. Experiments were not randomized. Investigators were not blinded to allocation during experiments and outcome assessment. Rosette resolution angles were measured by first assigning a rostrocaudal reference axis taken from a low ×10 confocal magnification view of the embryo flank. Rosettes were identified manually, frame-by-frame. The angle between the long axis of the ellipse outlined by each rosette and the reference axis was documented at the beginning of a given video and on resolution.

Laser ablation. Laser ablation was performed as described previously[63] with modifications to optimize for live mouse embryo culture. Briefly, *mTmG; Crect* embryos were placed in a 25 mm imaging chamber containing 50% rat serum in DMEM, and immobilized with cheese cloth. An N_2 Micropoint laser (Andor Technology) set to 365 nm was used to ablate cell interfaces. Images were acquired on an Andor Revolution XD spinning-disc confocal microscope attached to an iXon Ultra897 EMCCD camera (Andor Technology) using a ×60 oil-immersion lens (Olympus, NA 1.35). Vertices were identified manually using SIESTA software[30]. Annotated vertices were tracked and initial retraction velocities were calculated using an algorithm developed in Matlab (Mathworks)/DIPImage (TU Delft). Sample variances were compared using an *F*-test, and mean values were compared using Student's *t*-test with Holm's correction. To compare time series, the areas under the curves were used as the test statistic. Images were processed using ImageJ. Rosette aspect ratio was determined using the Fit Ellipse tool in ImageJ. Error bars indicate standard error of the mean and the *P* value was calculated using Student's *t*-test.

Inhibitor treatment. For Wnt inhibition, embryos were treated in roller culture[64] with 100 μM IWR-1, 50 μM IWP-2, or DMSO control in 50% rat serum in DMEM for 6 h, and then fixed in 4% paraformaldehyde overnight at 4 °C. For actin polymerization inhibition, embryos were treated in roller culture with 100 μM NSC23766 in 50% rat serum in DMEM for 3 h before live imaging in inhibitor-containing media.

PEG and collagen injections. E9.25 embryos were collected and placed in 6 cm dish coated with 2% agarose containing 5% FBS in DMEM. Embryos were immobilized using pulled glass needles to pin the head to the agarose. A second needle was pinned to the agarose and the tails of the embryos were carefully placed between the needle and the agarose, taking care not to puncture or damage the tissue. Embryos were injected with a 0.6 mg ml⁻¹ collagen or polyethylene glycol (PEG) diacrylate (M_n575) solution (10% solution containing 0.02% 2,2-dimethoxy-2-phenylacetophenone (DMPA) as a photocuring agent) containing 1 μg μl⁻¹ rhodamine–dextran in DMEM. For PEG injections embryos were placed under 365 nm ultraviolet light for 40 s to allow gel formation. The targeted region of injection was the lateral plate posterior to the forelimb bud, approximately at the level of somites 15–18. Embryos were then incubated in roller culture in 50% rat serum in DMEM for 4 h and fixed in 4% paraformaldehyde overnight at 4 °C.

Quantification of polarized actin distribution. Single confocal slices taken 2 μm above the basal surface of ectoderm cells stained with rhodamine–phalloidin were analysed using SIESTA software. Cell interfaces were manually identified, and average fluorescence intensities were calculated for all interfaces and grouped into 15° angular bins, using SIESTA software, with the 0°–15° bin representing interfaces that are parallel with the AP axis (DV interfaces) and the 75°–90° bin representing interfaces that are parallel with the DV axis (AP interfaces). Average fluorescence intensity values for each bin were normalized to average fluorescence intensity of DV interfaces (0°–15° angular bin). Error bars indicate standard error of the mean and *P* values were calculated using Student's *t*-test.

Quantification of cell behaviours. Metaphase-to-telophase transition angles were measured as described previously[6]. Angles of cell orientation were measured manually as the long axis of cells grouped in 15° bins over a 90° angular range. GFP-positive nuclei were quantified using average fluorescence intensity of GFP normalized to average fluorescence intensity of DAPI. Oscillation of cortical actin

contractions was quantified by measuring the length of interfaces labelled with Venus–actin frame-by-frame over 2 h and normalized to the maximum length of each interface. Relative rates of change of interface length were plotted over time and average peak amplitude was calculated for each interface. Meandering index and DV displacement were quantified using ImageJ for a 2 h time course. Meandering index was calculated as displacement/total distance travelled. Error bars represent standard error of the mean and the *P* value was calculated using Student's *t*-test.

Mouse lines. *CAG::myr–Venus*[35]; *CAG::H2B-GFP* (Jackson Laboratory, B6.Cg-Tg(HIST1H2BB/EGFP)1Pa/J); *Tcf/Lef::H2B–Venus*[26]; *mTmG* (Jackson Laboratory, *Gt(ROSA)26Sor^{tm4(ACTB–tdTomato,–EGFP)Luo}*/J); *R26R–Venus–actin* (Acc. No. CDB0218K, http://www.cdb.riken.jp/arg/reporter_mice.html[32]); *Crect*[33]; ZEG (Jackson Laboratory, *Tg(CAG–Bgeo/GFP)21/Lbe/J*); *β-catenin flox* (Jackson Laboratory, *B6.129-Ctnnb1^{tm2Kem}/KnwJ*); *Fgfr2 flox* (Jackson Laboratory, STOCK *Fgfr2^{tm1Dor}*/J). Genotyping primers are available on the Jackson Laboratory website for each mouse line. All mouse lines are outbred to CD1, with the exception of *β-catenin flox* and *Fgfr2 flox*, which are C57BL/6J background. To generate mutant embryos, flox/flox females carrying the appropriate fluorescent reporter were bred to *flox/+; Crect* males. All animal experiments were performed in accordance with protocols approved by the Hospital for Sick Children Animal Care Committee.

Whole-mount immunofluorescence. Embryonic day (E) 9.0–10.0 mouse embryos were fixed overnight in 4% paraformaldehyde in PBS followed by 3 washes in PBS. Embryos were permeabilized in 0.1% Triton X-100 in PBS for 20 min and blocked in 5% normal donkey serum (in 0.05% Triton X-100 in PBS) for 1 h. Embryos were incubated in primary antibody for 5 h at room temperature, followed by overnight incubation at 4 °C. Embryos were washed in 0.05% Triton X-100 in PBS (4 washes, 20 min each), and then incubated in secondary antibody for 3–5 h at room temperature. Embryos were washed (4 washes, 20 min each), followed by a final wash overnight at 4 °C, and stored in PBS. Images were acquired using a Quorum spinning-disc confocal microscope at ×10, ×20 or ×40 magnification, and image analysis was performed using Volocity software and ImageJ.

Antibodies. β-catenin (BD Biosciences 610153, mouse, 1:200); E-cadherin (BD Biosciences 610181, mouse, 1:250 immunofluorescence, 1:1,000 immunoblotting); myosin IIB (Covance PRB-445P, rabbit, 1:500); myosin IIA (Covance PRB-440P, rabbit, 1:500); phospho-myosin light chain 2 (Thr18/Ser19) (Cell Signaling 3671, rabbit, 1:250); phospho-ERK1/2 (Thr202/Tyr204) (Cell Signaling 4370, rabbit, 1:500); CD44 (eBioscience 14-0441, rat, 1:500); phospho-histone H3 (Cell Signaling 9706, mouse, 1:250); caspase3 (BD Bioscience 559565, rabbit, 1:250); Dishevelled 3 (Santa Cruz sc-8027, mouse, 1:200); Frizzled 6 (R&D Systems AF1526, goat, 1:200); phospho- β-catenin (Abcam ab24925, mouse, 1:200); Dishevelled 2 (Santa Cruz sc-10B5, mouse, western blotting 1:500); Par1 (Abcam ab77698, mouse, 1:200); Par3 (Millipore 07-330, rabbit, 1:200); rhodamine–phalloidin (Invitrogen, 1:1,000). All secondary antibodies were purchased from Jackson Immunoresearch and used at 1:1,000 dilutions.

Whole-mount *in situ* hybridization. Whole-mount *in situ* hybridization was performed as described previously[64]. Wild-type and mutant littermates, and IWR-1-treated and control DMSO-treated embryos were processed identically in the same assay for comparison. *Axin2* (ref. 65) and *Fgf10* (ref. 66) riboprobes were previously described.

Western blotting. Embryos treated with IWP-2 or DMSO control were lysed in PLC lysis buffer (50 mM HEPES pH 7.5, 150 mM NaCl, 1.5 mM $MgCl_2$, 1 mM EGTA, 10% glycerol, 1% Triton X-100, protease inhibitors (Roche)). Proteins were separated by SDS–PAGE, transferred to PVDF membranes (PerkinElmer), and incubated with primary antibodies overnight at 4 °C. Immunoblots were developed using HRP-conjugated secondary antibodies (Santa Cruz) and ECL (PerkinElmer).

Optical projection tomography. E9.5 mouse embryos were collected and fixed in 4% paraformaldehyde overnight at 4 °C. Optical projection tomography (OPT) was performed essentially as previously published. The OPT system was custom-built and is fully described elsewhere[67]. The three-dimensional (3D) data sets were reconstructed from auto-fluorescence projection images acquired over a 10 min scan time at an isotropic voxel size of 3.85 μm. The 3D surface renderings of the OPT data were generated by Amira software, version 5.3.3 (VSGG).

Atomic force microscopy. Embryos were incubated in 50% rat serum in DMEM on a 35 mm dish in which 2% agarose was poured around the perimeter. Embryos were immobilized to the agarose with pulled glass needles pinned through the flank adjacent to the limb field. Embryos were examined using a commercial AFM (BioScope Catalyst, Bruker) mounted on an inverted optical microscope (Nikon Eclipse-Ti).

Force-indentation measurements were undertaken using a spherical tip at distinct locations categorized as distal, middle and proximal limb bud with an indentation rate of 1 Hz. Spherical tips were made by assembling a borosilicate glass microsphere (radius: 5–10 μm) onto an AFM cantilever using epoxy glue. The cantilever (MLCT-D, Bruker) had a nominal spring constant of 0.03 N m⁻¹. The trigger force applied to the embryo limb bud was consistently 200 pN, which helped to exclude erroneously high Young's moduli arising from the influence of the underlying cell layers. Hence, no explicit correction for finite sample thickness effects was made here, and no evidence of depth-dependent stiffening was observed. The Hertz model was applied to the force curves to estimate the Young's modulus and contact point, which were further used to convert the force curves into stress-indentation plots. We repeated indentation at the same location of the limb bud five times and observed no significant change in Young's moduli. As Young's modulus calculated from the Hertz model is sensitive to the spring constant, cantilever spring constants were calibrated each time before running the experiment by measuring the power spectral density of the thermal noise fluctuation of the unloaded cantilever. Detailed methods regarding use of a spherical tip and data analysis are described elsewhere[68].

Finite-element modelling. Finite-element modelling allowed us to focus on the mechanical behaviour of the ectodermal layer as a continuum with homogeneous viscoelastic material properties, rather than as individual cells. Viscoelastic behaviour was modelled using the Maxwell–Wiechert model[69]. The ectodermal tissue layer was assigned instantaneous elastic moduli of 0.085 kPa for wild type and 0.042 kPa for β-catenin mutant based on measurements taken using standard AFM indentation methods[68] and Poisson's ratio of 0.4 (ref. 70). Viscous relaxation of ectodermal modulus was calculated based on limb bud compression relaxation data reported previously[38] and was implemented in ANSYS as two-pair Prony relaxation with relative moduli of 0.1 and 0.4 and relaxation time constants of 8 s and 45 s, respectively.

Two types of mechanical load were considered: mesoderm growth was modelled as pressure (0.01 Pa) normal to the inner surface of the ectodermal pocket (analyses were performed for both shallow (17 som.) and tall (22 som.) models (Supplementary Fig. 1i,m,n)); AER progenitor intercalation at the DV boundary was modelled as equal and opposite pulling forces (2 pN) parallel to the DV axis at the junction of dorsal/ventral sides of the limb bud model (this analysis was performed only for the tall model (Supplementary Fig. 1n)). Two boundary conditions were used: for all simulations, four sides of the sheet were fixed in all six DOFs ($U_x = U_y = U_z = U_{Rx} = U_{Ry} = U_{Rz} = 0$), as the ectoderm at those locations was confined by connection to adjacent tissue; for simulation of AER progenitor cell intercalation, a frictionless support underneath the limb bud pocket was added that

reflects mesodermal support normal to the ectodermal plane and allows in-plane tangential displacement.

Geometries in each simulation were discretized using ten-node tetrahedral elements (C3D10) and the magnitudes of various loads used for simulation were within the physiological range of intercellular forces[43]. By varying simulated pulling forces at the prospective AER, we showed, as expected, that stress and deformation magnitude were linearly proportional to the load applied. Qualitative characteristics of stress pattern such as direction and ratio of principal stresses were similar despite different load magnitudes (Supplementary Fig. 1o,p). As the viscoelastic properties we inferred from previous compression data probably represent material tissue properties rather than dynamic cell rearrangements that might dissipate stress over time, our transient viscoelastic simulations probably do not accurately reflect fluid-like tissue physics over longer timescales. Stress dissipation due to cellular spatial rearrangements or relaxation can possibly explain why our transient FEA model predicted higher stress anisotropy in both distal and proximal limb bud regions compared with our laser ablation data that implied only the distal limb bud region exhibited significant tension bias. Nonetheless, finite-element modelling provided insight into how specific biological phenomena such as mesodermal cell growth and ectodermal cell intercalation influence the stress pattern across the limb field.

63. Fernandez-Gonzalez, R., Simoes Sde, M., Roper, J. C., Eaton, S. & Zallen, J. A. Myosin II dynamics are regulated by tension in intercalating cells. *Dev. Cell* **17,** 736–743 (2009).
64. Wyngaarden, L. A. & Hopyan, S. Plasticity of proximal-distal cell fate in the mammalian limb bud. *Dev. Biol.* **313,** 225–233 (2008).
65. Jho, E. H. *et al.* Wnt/β-catenin/Tcf signaling induces the transcription of Axin2, a negative regulator of the signaling pathway. *Mol. Cell. Biol.* **22,** 1172–1183 (2002).
66. Bellusci, S., Grindley, J., Emoto, H., Itoh, N. & Hogan, B. L. Fibroblast growth factor 10 (FGF10) and branching morphogenesis in the embryonic mouse lung. *Development* **124,** 4867–4878 (1997).
67. Wong, M. D., Dazai, J., Walls, J. R., Gale, N. W. & Henkelman, R. M. Design and implementation of a custom built optical projection tomography system. *PLoS ONE* **8,** e73491 (2013).
68. Liu, H., Sun, Y. & Simmons, C. A. Determination of local and global elastic moduli of valve interstitial cells cultured on soft substrates. *J. Biomech.* **46,** 1967–1971 (2013).
69. Kaufman, J. D., Miller, G. J., Morgan, E. F. & Klapperich, C. M. Time-dependent mechanical characterization of poly(2-hydroxyethyl methacrylate) hydrogels using nanoindentation and unconfined compression. *J. Mater. Res.* **23,** 1472–1481 (2008).
70. Trickey, W. R., Baaijens, F. P., Laursen, T. A., Alexopoulos, L. G. & Guilak, F. Determination of the Poisson's ratio of the cell: recovery properties of chondrocytes after release from complete micropipette aspiration. *J. Biomech.* **39,** 78–87 (2006).
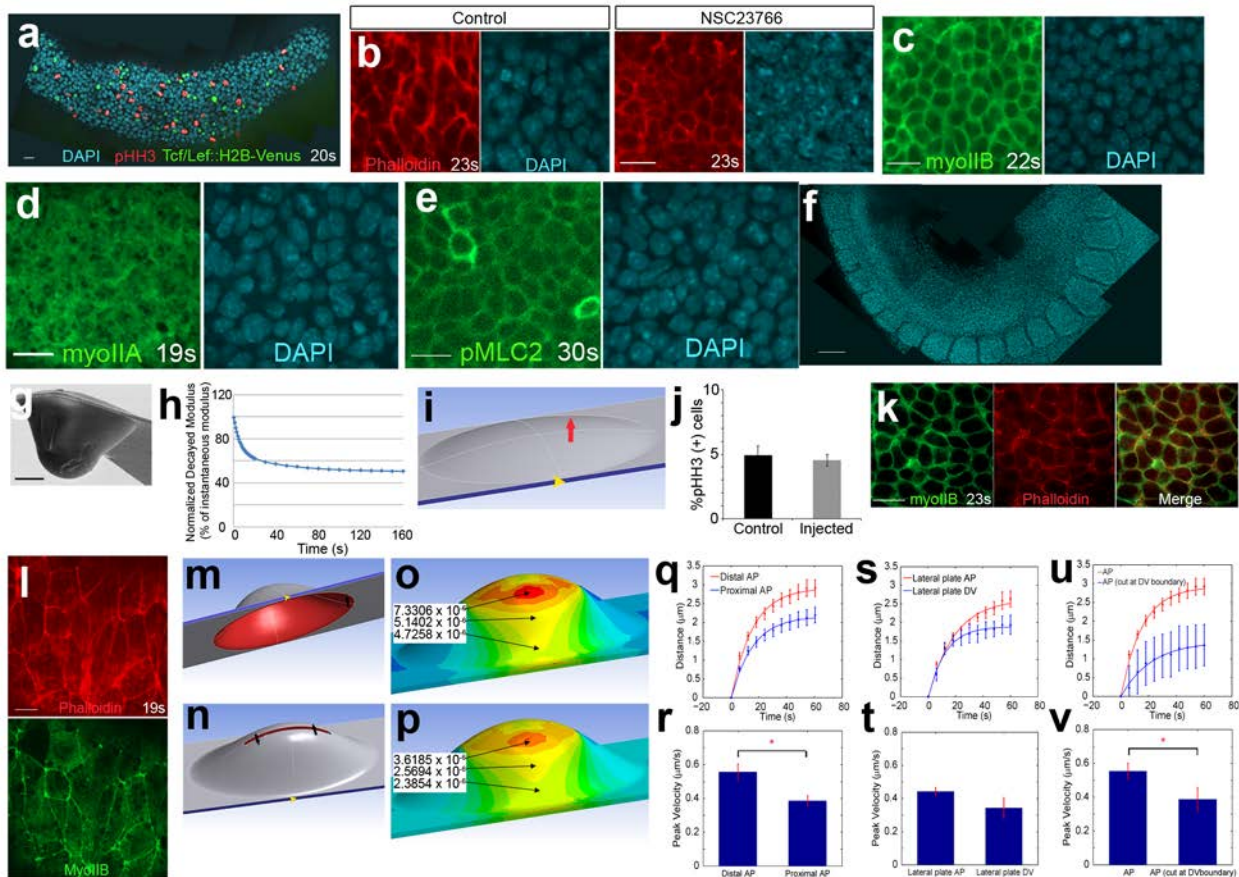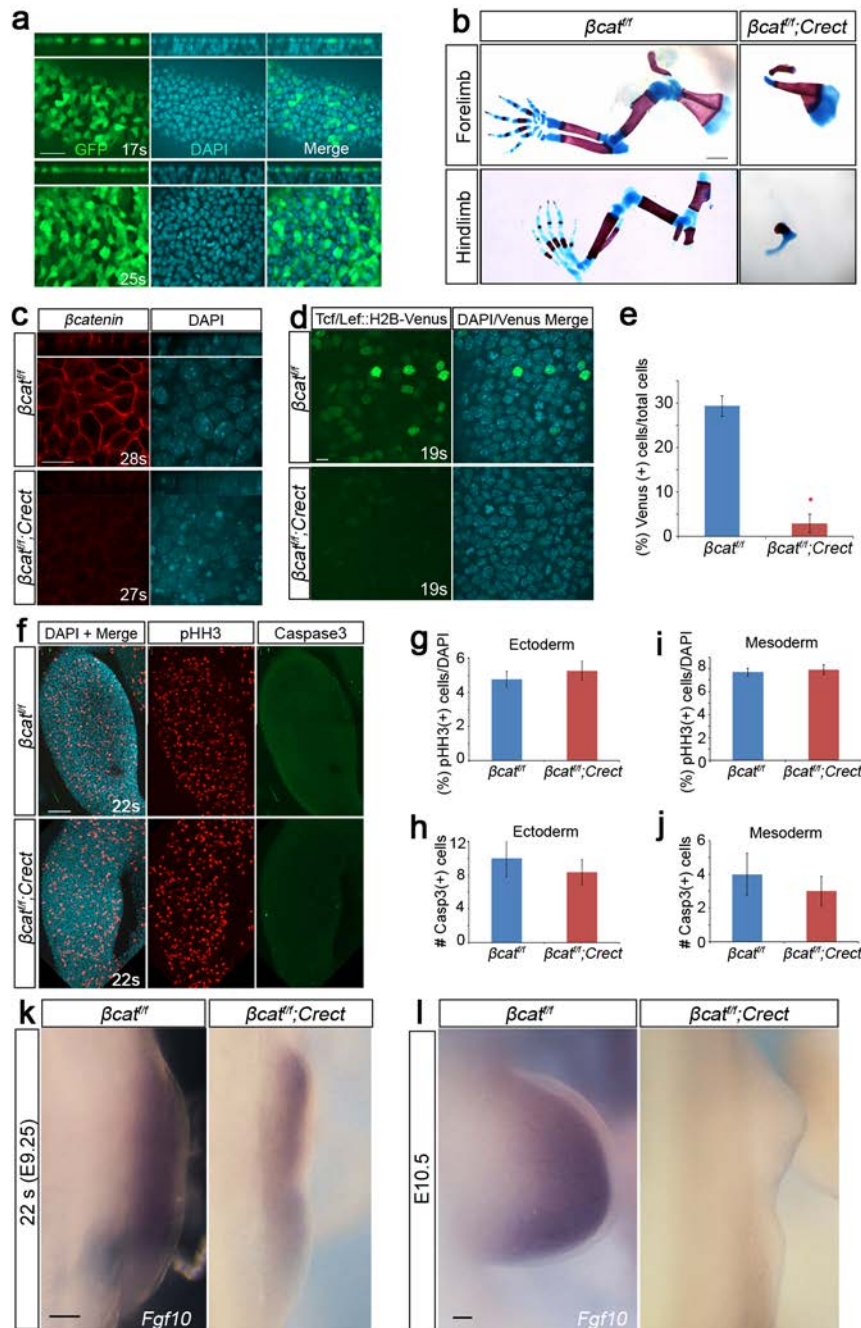
Supplementary Figure 1 (a) Confocal projection of 20s limb bud visualising pHH3 (red), Tcf/Lef::H2B-Venus (green), and DAPI (blue). Shown are multiple images stitched together. (b) *xy* sections of limb field in embryos treated with water control (left) or 100 μM NSC23766 (right) visualising actin (red) and DAPI (blue). (c-e) *xy* sections at the DV boundary of initiating limb bud ectoderm visualising Myosin IIB (c), Myosin IIA (d), phospho-Myosin Light Chain-1 (e) (green) and DAPI (blue). (f) Composite confocal projection of 17-somite stage lateral plate visualising DAPI used to measure dimensions of pre-limb lateral plate ectoderm for simulation. (g) Scanning electron micrograph of a custom 10 μm spherical AFM probe. (h) Two-paired Prony series fitting of limb bud viscoelastic properties. (i) Illustration of finite element model of initiating limb bud. Red arrow indicates direction of mesodermal growth, yellow arrowhead indicates fixed support. (j) Percentage of pHH3-positive cells relative to total cells in control versus PEG-injected embryos (n=3 18-21 som. embryos; p=0.9871 (Student's *t*-test)). (k) *xy* section away from DV boundary of pre-AER 23 som. limb bud ectoderm

visualising Myosin IIB (green) and Actin (red). (l) *xy* section of the apical plane of 19 som. limb bud visualising actin (red) and myosin (green). (m) Model of 22 som. pre-AER limb bud. Black arrow indicates mesodermal growth, yellow arrowhead indicates fixed support. (n) Model of AER progenitor intercalation at DV boundary. Black arrows indicate direction of ectodermal tension (modelled as pulling force). (o,p) Stresses are linearly proportional to the pulling force applied at the DV midline; (o) 2 pN, (p) 1 pN. (q,s,u) Distance between two vertices attached to cut interface for (q) distal AP versus proximal AP, p=0.0142, (s) lateral plate AP versus lateral plate DV, p=0.1381, (u) intact AP versus post-cut AP interfaces, p=0.0475. (r,t,v) Peak retraction velocities of ablated (r) distal AP versus proximal AP, (t) lateral plate AP versus lateral plate DV, (v) AP versus post-cut AP interfaces ((r) p=0.0023, (t) p=0.1544, (v) p=0.0488; (q-v) n~15 ablations for each of 4 embryos). ((q-r) Student's *t*-test with Holm's correction). Scale bars indicate 5 μm (g), 10 μm (c-e, k,l), 20 μm (a,b), 100 μm (f). Error bars indicate SEM.
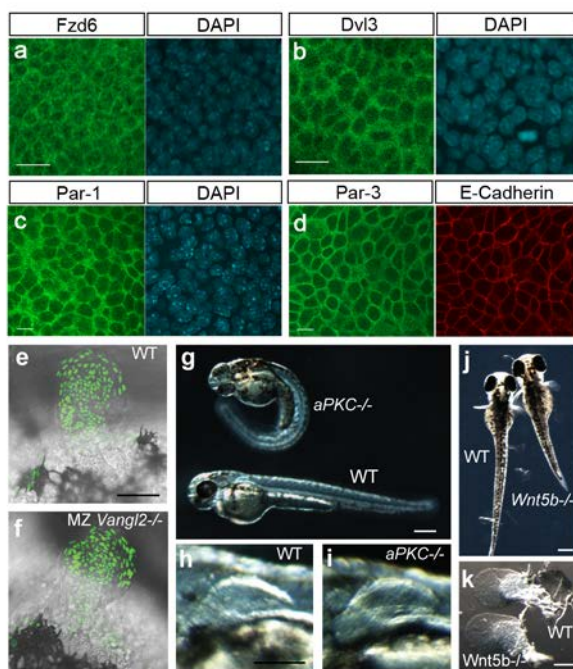
Supplementary Figure 2 (a) Confocal *xy* section of initiating limb bud ectoderm visualising Frizzled6 (green) and DAPI (blue). (b) Confocal *xy* section of initiating limb bud ectoderm visualising Disheveled3 (green) and DAPI (blue). (c,d) Confocal xy section of initiating limb bud ectoderm visualizing Par1 (green) and DAPI (blue) (c) and Par3 (green) and E-cadherin (red) (d). In all images, scale bar indicates 20 μm; anterior is left and ventral is up. (e) Wildtype and (f) Maternal zygotic (MZ) *Vangl2*-/- 56 hpf zebrafish pectoral fin bud visualising *H2B-GFP* nuclei (green). (g) Wildtype and *aPKC*-/- 34 hpf zebrafish embryos. (h) Wildtype and (i) *aPKC*-/- zebrafish pectoral fin bud. (j) Wildtype and *Wnt5b*-/- 96 hfp zebrafish embryos. (k) Wildtype and *Wnt5b*-/- zebrafish pectoral fin bud. Scale bars indicate (20 μm (a,b), 10 μm (c,d), 100 μm (e,f, h,i,k), 250 μm (g,j).
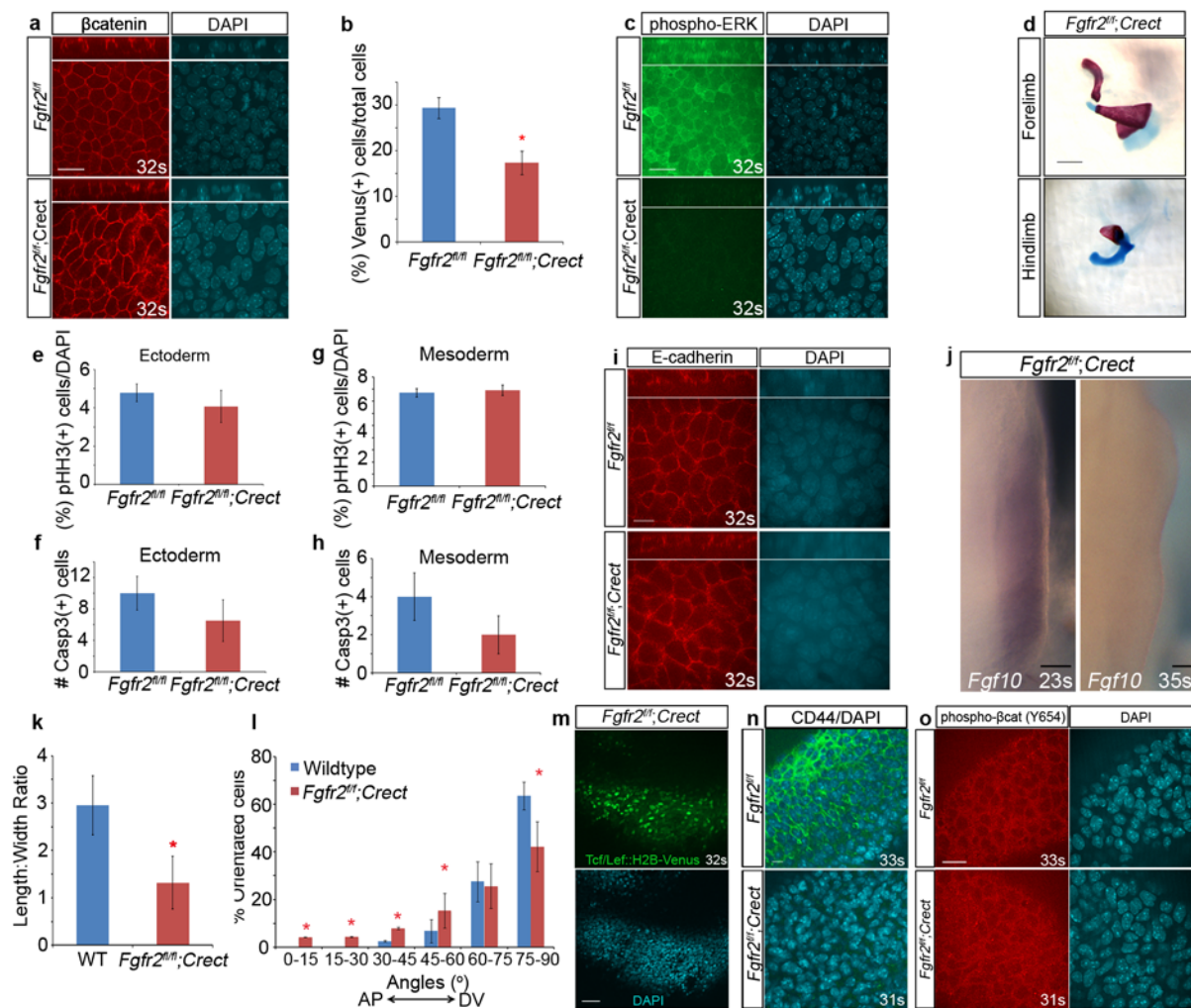
Supplementary Figure 3 (a) Confocal *z* sections and *xy* sections of *ZEG;Crect* limb buds at 17 som. stage (E9.0) (top) and 25 som. stage (E9.5) (bottom) visualising GFP (green) and DAPI (blue). (b) Cartilage (Alcian Blue) and bone (Alizarian Red) staining of E18.5 WT and βcat*f/f;Crect* mutant forelimb (top panels) and hindlimb (bottom panels) skeletons. (c) Confocal *z* sections (top panels) and *xy* sections (bottom panels) of control βcat*f/f* and βcat*f/f;Crect* mutant limb bud ectoderm visualising β-catenin (red) and DAPI (blue). (d) Confocal *xy* sections of control βcat*f/f* and βcat*f/f;Crect* mutant limb bud ectoderm expressing *Tcf/ Lef::H2B-Venus*. Shown are GFP (green) and DAPI (blue). (e) Histogram representing percentage GFP-positive nuclei in control βcat*f/f* and βcat*f/f;Crect* mutant limb bud ectodermal cells expressing *Tcf/Lef::H2B-Venus* (p = 1.7 x 10⁻⁵ (Student's *t*-test); n=3 19-25 som. embryos). (f) Confocal projection of control βcat*f/f* and βcat*f/f;Crect* mutant limb bud ectoderm visualizing phospho-histone H3 (red), Caspase3 (green), and DAPI (blue). (g) Histogram representing percentage of pHH3-positive cells in control βcat*f/f* and βcat*f/f;Crect* mutant limb bud ectodermal cells (p=0.8956). (h) Histogram representing number of Caspase3-positive cells in control βcat*f/f* and βcat*f/f;Crect* mutant limb bud ectodermal cells (p=0.8413). (i) Histogram representing percentage of pHH3-positive cells in control βcat*f/f* and βcat*f/f;Crect* mutant limb bud mesodermal cells (p=0.9671). (j) Histogram representing number of Caspase3-positive cells in control βcat*f/f* and βcat*f/f;Crect* mutant limb bud mesodermal cells (p=0.7691). (For g-j n= 3 19-21 som. embryos per condition, Student's *t*-test) (k) *Fgf10* expression in control βcat*f/f* and βcat*f/f;Crect* mutant limb buds at 22 som. (E9.25). (l) *Fgf10* expression in control βcat*f/f* and βcat*f/f;Crect* mutant limb buds at E10.5. Scale bar indicates 10 μm (a,c,d), 100 μm (f,k,l), 1mm (b). Error bars indicate SEM. Asterisk indicates p<0.05.
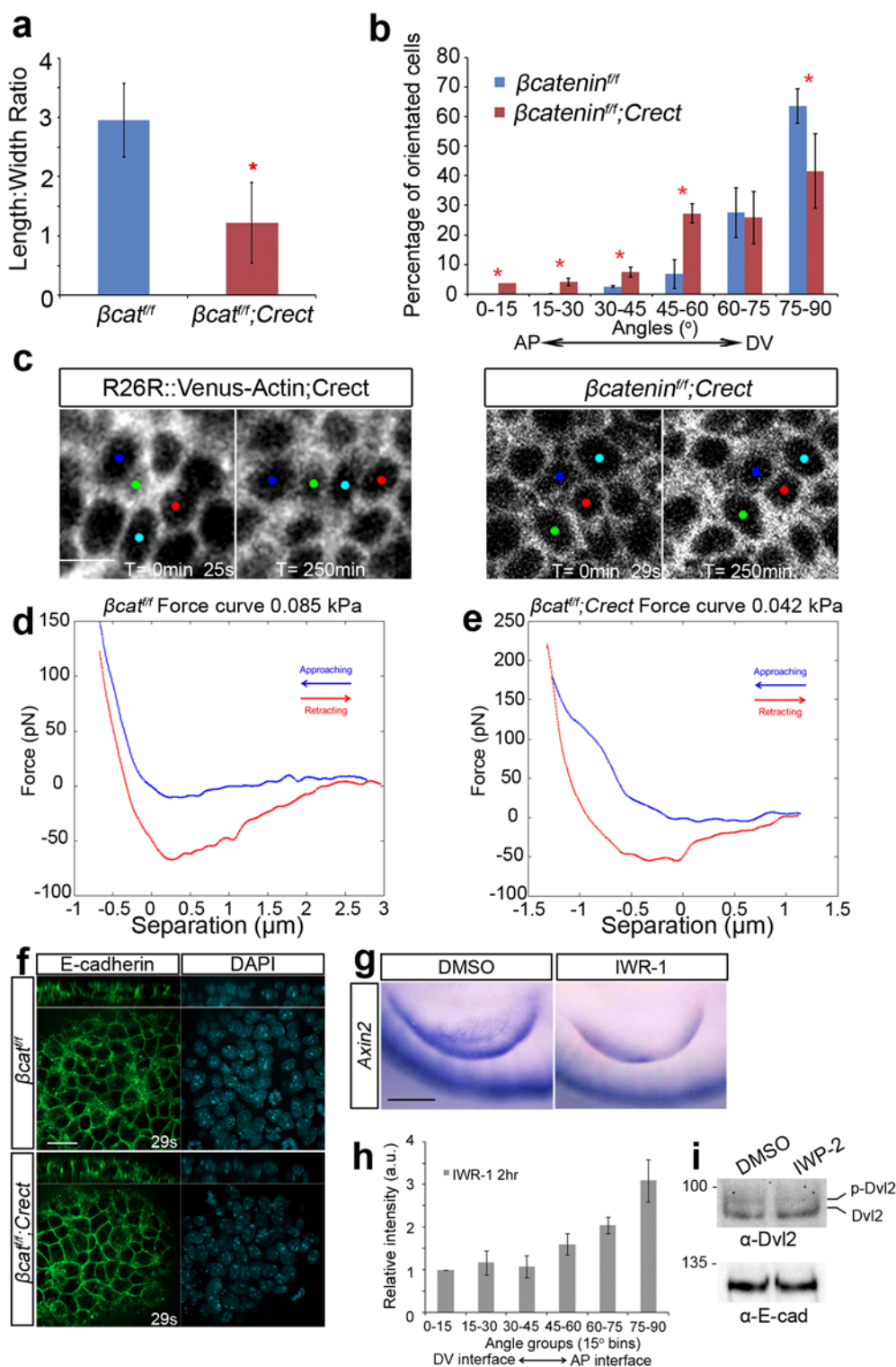
Supplementary Figure 4 (a) Length-width ratio of control βcat$^{f/f}$ and βcat$^{f/f}$;Crect mutant limb bud ectodermal cells. (n=3 19-21 som. embryos per condition; p=0.0324 (Student's *t*-test)) (b) Angle of cell orientation in control βcat$^{f/f}$ and βcat$^{f/f}$;Crect mutant limb bud ectoderm. Histogram shows distribution of cells grouped into 6 bins of 15°(n=3 19-21 som. embryos per condition; p=0.0332 (75-90° bin) (Student's *t*-test)). (c) Time series of initiating limb bud ectoderm cells in WT and βcat$^{f/f}$;Crect mutant embryos expressing *R26R::Venus-Actin*. (d,e) Representative force curves for control βcat$^{f/f}$ (d) and βcat$^{f/f}$;Crect (e) mutant AFM experiments. (f) Confocal XY section of control βcat$^{f/f}$ and βcat$^{f/f}$;Crect mutant limb bud ectoderm visualizing E-cadherin (green) and DAPI (blue). (g) *Axin2* expression in embryos that were treated in 6-hour roller culture with DMSO control (top) or IWR-1 (bottom). (h) phospho-Dishevelled 2 (p-Dvl2) is diminished in embryos treated with IWP-2. Uncropped blots in Supplementary Fig. 6. Scale bar indicates 20 μm (c,f), 200 μm (g); anterior is left and ventral is up. Error bars indicate SEM. Asterisk indicates p<0.05.

Supplementary Figure 5 (a) Confocal Z sections (top panels) and XY sections (bottom panels) of control *Fgfr2^{f/f}* and *Fgfr2^{f/f};Crect* mutant limb bud ectoderm visualising βcatenin (red) and DAPI (blue). (b) Histogram representing percentage Venus-positive nuclei from *Fgfr2^{f/f}* and *Fgfr2^{f/f};Crect* mutant limb bud ectodermal cells expressing *Tcf/Lef::H2B-Venus* (p = 0.0014 (Student's *t*-test); WT n=3, mutant n=4 20-25 som. embryos). (c) Confocal XY section of *Fgfr2^{f/f}* and *Fgfr2^{f/f};Crect* mutant limb bud ectoderm visualising phospho-ERK (green) and DAPI (blue). (d) Cartilage (Alcian Blue) and bone (Alizarian Red) staining of E18.5 *Fgfr2^{f/f};Crect* mutant forelimb (top) and hindlimb (bottom) skeletons. (e) Histogram representing percentage of pHH3-positive cells in *Fgfr2^{f/f}* and *Fgfr2^{f/f};Crect* mutant limb bud ectodermal cells (p=0.8731). (f) Histogram representing number of Caspase3-positive cells in *Fgfr2^{f/f}* and *Fgfr2^{f/f};Crect* mutant limb bud ectodermal cells (p=0.6567). (g) Histogram representing percentage of pHH3-positive cells in *Fgfr2^{f/f}* and *Fgfr2^{f/f};Crect* mutant limb bud mesodermal cells (p=0.9973). (h) Histogram representing number of Caspase3-positive cells in *Fgfr2^{f/f}* and *Fgfr2^{f/f};Crect*

mutant limb bud mesodermal cells (p=0.6032). (For e-h, n=3 19-21 som. embryos per condition, Student's *t*-test) (i) Confocal XY section of *Fgfr2^{f/f}* and *Fgfr2^{f/f};Crect* mutant limb bud ectoderm visualising E-cadherin (red) and DAPI (blue). (j) *Fgf10* expression in *Fgfr2^{f/f};Crect* mutant limb buds at E9.5 (left) and E10.5 (right). (k) Length-width ratio of WT and *Fgfr2^{f/f};Crect* mutant limb bud ectodermal cells (n=e 19-21 som. embryos per condition; p=0.0189 (Student's *t*-test). (l) Angle of cell orientation in WT and *Fgfr2^{f/f};Crect* mutant limb bud ectoderm. Histogram shows distribution of cells grouped into 6 bins of 15°(n=3 19-21 som. embryos per condition; p=0.0412 (75-90° bin) (Student's *t*-test)). (m) Confocal XY projection of E10.0 (32 somite stage) *Fgfr2^{f/f};Crect* mutant forelimb bud expressing *Tcf/Lef::H2B-Venus*. (n) Confocal images of *Fgfr2^{f/f}* and *Fgfr2^{f/f};Crect* mutant limb bud ectoderm visualising CD44 (green) and DAPI (blue). (o) Confocal XY sections *Fgfr2^{f/f}* and *Fgfr2^{f/f};Crect* mutant limb bud ectoderm visualizing phospho-βcatenin (red) and DAPI (blue). Scale bar indicates 20 μm (a,c,o), 10 μm (i,n), 50 μm (m), 100 μm (j), 1mm (d). Error bars indicate SEM. Asterisk indicate p<0.05.
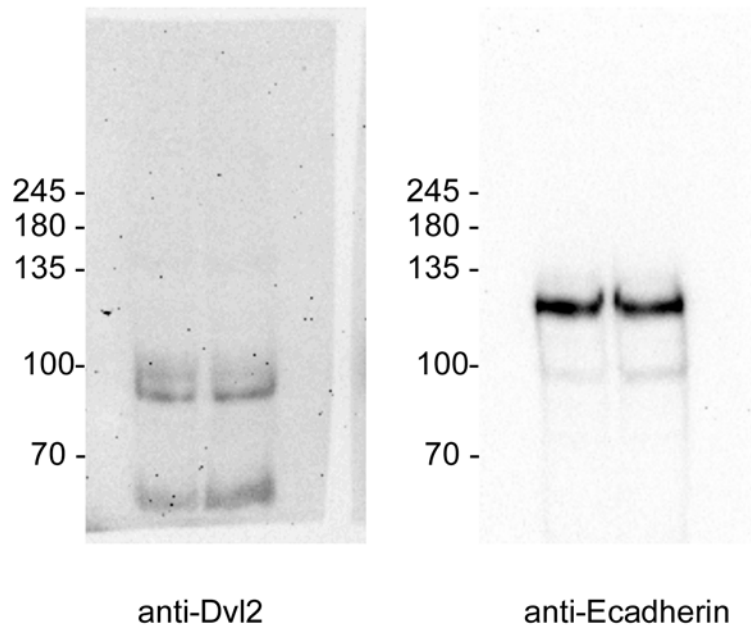
Supplementary Figure 6 Uncropped Western blot showing reduced levels of p-Dvl2 in IWP-2 treated embryos compared with control DMSO treatment. (Right) Re-blot of E-cadherin as loading control.

SUPPLEMENTARY INFORMATION

Supplemental video Legends

Supplementary video 1 DV movement of *Tcf/Lef::H2B-Venus*-positive cells in ventral ectoderm of a 23 som. stage limb bud. Shown is a lateral view of the posterior half of the limb bud. Anterior is to the left, dorsal is down. Time course is 165 min, shown in 5 fps. Evidence of convergence by intercalation can be seen, as can DV-biased cell division planes. Over a longer time period (nearly 1 day), these cells will progressively crowd just ventral to the DV midline to form the AER.

Supplementary video 2 *Tcf/Lef::H2B-Venus*-positive cells at 23 som. stage intercalate just ventral to the dorsoventral boundary (in our estimation). Anterior is to the left; dorsal is down. Time course is 165 min, shown in 5 fps.

Supplementary video 3 Low magnifcation time lapse movie demonstrating interdigitation of *Tcf/Lef::H2B-Venus*-positive cells (precipitated by division of the light blue cell) near the DV midline of a 20 som. stage limb bud. Anterior is to the left, dorsal is downward, and ventral is upward. Time course is 355 min, shown in 5 fps.

Supplementary video 4 Wild type 20 som. *myr-Venus* transgenic embryo with a dorsally biased view of anterior half of limb field (left half) and lateral plate ectoderm (right half). Polygonal, anisotropic cell shapes dominate, and multiple examples of cell division and cell neighbour exchange are apparent. Anterior is to the right and dorsal is downward with the DV midline ~2/3 up from the base of the visible field.

Supplementary video 5 NSC23766 treatment of 22 som. stage *myr-Venus* embryo demonstrates transition from elongated cell shapes to more isotropic shapes. Diminished cell neighbour exchange is also apparent. Time course is 75 min, shown in 5 fps.

Supplementary video 6 Protrusive membrane activity of ectodermal cells in 22 som. limb bud expressing *myr-Venus* in a mosaic fashion. Yellow arrowhead indicates membrane protrusion. To the left, a relatively dark cell intercalates among two bright cells. Anterior is to the left and dorsal is downward. Time course is 180 min, shown in 5fps.

Supplementary video 7 Relaxation of principal stress vectors during transient 300 s viscoelastic simulation for 17 som. stage limb bud initiation based on mesodermal growth. All principal stresses are relaxed until the material property reaches the asymptote. Same relaxation applies to the stress field (not shown).

Supplementary video 8 Daughter cells (blue) in mouse embryonic ectoderm (20 som.) frequently sever the interface between them immediately following division and precipitate neighbour exchange. Anterior is left; dorsal, down. Time course is 149 min, shown in 5 fps.

Supplementary video 9 A daughter cell (blue) intercalates between neighbouring cells following division (20 som.). Anterior is left; dorsal, down. Time course is 149 min, shown in 5 fps.

Supplementary video 10 A daughter cell (pink) precipitates rosette formation by intercalating between cells and contributes to the central apex (20 som.). Anterior is left; dorsal, down. Time course is 83 min, shown in 5 fps.

Supplementary video 11 A large multicellular rosette resolves into two rows of cells by dissolving its central apex and generating new intercellular junctions (20 som.). Anterior is left; dorsal, down. Time course is 123 min, shown in 5 fps.

Supplementary video 12 Relaxation of the stress field during transient 300 s viscoelastic simulation for 22 som. stage pre-AER limb bud due to mesodermal growth.

Supplementary video 13 Relaxation of the stress field during transient 300 s viscoelastic simulation for 22 som. stage pre-AER limb bud due to an ectodermal pulling force at the DV midline.

Supplementary video 14 Precise laser ablation of a single AP interface (that is parallel to the DV axis) results in relatively fast initial recoil of adjacent apices along the DV axis (21 som.). Anterior is left. Time course is 132 sec, shown in 5 fps.

Supplementary video 15 Precise laser ablation of a single DV interface (that is parallel to the AP axis) results in relatively slow initial recoil of adjacent apices along the AP axis (21 som.). Dorsal is left. Time course is 132 sec, shown in 5 fps.

Supplementary video 16 Laser ablation of multiple interfaces between the coloured rosette and the prospective AER (to the right) results in resolution of the rosette along the AP axis (up/down) rather than toward the AER (21 som.). Anterior is up; dorsal is left. Time course is 192 sec, shown in 5 fps.

Supplementary videoe 17 $\beta cat^{f/f};Crect$ mutant daughter cells maintain a long interface following division. Anterior is left; dorsal, down (20 som.). Time course is 135 min, shown in 5 fps.

Supplementary video 18 $\beta cat^{f/f};Crect$ mutant rosette resolves with minimal angular change of its long axis. Anterior is left; dorsal, down (20 som.). Time course is 140 min, shown in 5 fps.

Supplementary video 19 Live *R26R::Venus-Actin* reporter in vivo shows oscillatory cortical contractions in wild type embryo. Anterior is left; dorsal, down. Time course is 120 min, shown in 5 fps.

Supplementary video 20 Live *R26R::Venus-Actin* reporter in vivo shows diminished amplitude and rate of change of oscillatory cortical contractions in $\beta cat^{f/f};Crect$ mutant embryo (21 som.). Anterior is left; dorsal, down. Time course is 120 min, shown in 5 fps.

Supplementary videoe 21 Tcf/Lef::H2B-Venus positive cells in *Fgfr2^{f/f};Crect* mutant limb bud ectoderm move along the DV axis, albeit less efficiently than in WT (21 som.). Anterior is left; dorsal, down. Time course is 120 min, shown in 5 fps.